

Copyright
by
Daniel Moncrief Tennant
2017

The Dissertation Committee for Daniel Moncrief Tennant
certifies that this is the approved version of the following dissertation:

**Aging as a Measure of Domain Growth in Multilayer
Thin Films of the Spin Glass Copper Manganese**

Committee:

Raymond L. Orbach, Supervisor

John T. Markert, Co-Supervisor

Gregory G. Kenning

Michael P. Marder

Allan H. MacDonald

**Aging as a Measure of Domain Growth in Multilayer
Thin Films of the Spin Glass Copper Manganese**

by

Daniel Moncrief Tennant

DISSERTATION

Presented to the Faculty of the Graduate School of
The University of Texas at Austin
in Partial Fulfillment
of the Requirements
for the Degree of

DOCTOR OF PHILOSOPHY

THE UNIVERSITY OF TEXAS AT AUSTIN

December 2017

Dedicated to Lynne Cowles, who showed me how to write a thesis

Acknowledgments

I have many people to thank who have helped me along this journey. I have to especially thank all of my advisors along the way: Gerardo Muñoz, who really taught me the craft, John Markert, and all of the Freshman Research Initiative, who provided me a home here at the university, Gregory Kenning, who I learned how to be an experimentalist from, and finally Raymond Orbach, who not only opened many doors for me, taught me how to successfully herd cats, but especially how to have fun while doing it all. I am very grateful to all of my lab mates who, along the way, became my life mates: Jeremy Pastor, Gregorio Ponti, and especially Shirin Mozaffari. I had the chance to befriend a number of incredible people, too many to mention all, but they've all helped me celebrate the ups and get me through the downs of this experience. My footballing communities, ATX United, the Subalterns, and the Competitive Excluders have all provided a healthy layer to my time here. Thank you to all of my siblings for being supportive of me, helping me with all the broken down trucks, and just always being there to share a drink and story, and especially to both of my parents, my original teachers.

Aging as a Measure of Domain Growth in Multilayer Thin Films of the Spin Glass Copper Manganese

Publication No. _____

Daniel Moncrief Tennant, Ph.D.

The University of Texas at Austin, 2017

Supervisor: Raymond L. Orbach

Co-Supervisor: John T. Markert

This work describes two related investigations into the spin glass phase of $\text{Cu}_{0.88}\text{Mn}_{0.12}$ multilayer thin films. In addition, the construction of and improvements on a home built SQUID magnetometer built in pursuit of these goals will be detailed. The common theme between these experiments at the mesoscale is the exploitation of the fact that the film thickness and the length scale of spin glass correlations are of comparable size. The fact that the lower critical dimension of the spin glass phase is between two and three allows a direct probe of the transition between a finite temperature phase transition and zero temperature fixed point glassy state. The time and temperature dependence of the correlation length growth as well as the energy barrier structure is explored and found to agree with the predictions of the hierarchical model of Parisi and is at odds with the droplet model of Fisher and Huse. In particular, the growth of correlations is cut off by the finite film thickness. This results in

a maximum energy barrier in configuration space dictated by the film thickness and independent of temperature. In addition, the growth of domains, or correlated regions, is explored through the waiting time effect in the Thermoremanent Magnetization decays. Aging, or the exploration of configuration space through thermally activated transitions, is shown to be directly related to the growth of domains in this disordered system.

Table of Contents

Acknowledgments	v
Abstract	vi
List of Tables	x
List of Figures	xi
Chapter 1. Introduction	1
1.1 Experimental History	2
1.2 Theoretical Developments	8
1.2.1 Previous Work on Spin Glass Thin Films	13
Chapter 2. Glassy Dynamics in Spin Glass Multilayer Thin Films	19
Chapter 3. Experimental Apparatus	32
3.1 Experimental Apparatus	39
3.1.1 Structure of the Probe	41
3.1.2 Sample Holder and Temperature Control System	43
3.1.3 Squid, Pick up Coil, and Magnet Assembly	45
3.2 Experimental Protocol and Results	50
Chapter 4. Aging as Domain Growth	57
4.1 Experimental Techniques	58
4.2 Experimental Results	67
4.3 Discussion	68
Chapter 5. Conclusion	85
Bibliography	88

List of Tables

2.1	$\Delta_{\max}(\mathcal{L})/k_B$ extracted at different temperatures for each multilayer CuMn thin film.	24
4.1	Values for c_1 and c_2 over a range of experiments.	72

List of Figures

1.1	Cu _{0.96} Mn _{0.04} Field Cooled and Zero Field Cooled Magnetization.	4
1.2	Cu _{1-x} Mn _x Specific Heat with $T_g = 3$ K [10]	5
1.3	Cu _{0.96} Mn _{0.04} $T_m = 23.4$ K. The $S(t) = \frac{\partial M(t, t_w, T)}{\partial \ln(t)}$ tracks the inflection point of the <i>TRM</i> on a logarithmic time scale. . . .	7
1.4	Freezing Temperatures of various concentrations and film thicknesses of Cu _{1-x} Mn _x [47]	14
1.5	$M_{FC} - M_{ZFC}$ in Ge _{0.89} Mn _{0.11} at various temperatures. $T_f = 24$ K 17	17
2.1	Cu _{0.88} Mn _{0.12} FC-ZFC for 4.5, 9, and 20 nm multilayer films . .	22
2.2	Cu _{0.88} Mn _{0.12} FC-ZFC for 4.5, 9, and 20 nm multilayer films . .	23
2.3	Cu _{0.88} Mn _{0.12} FC and ZFC for 4.5, 9, and 20 nm multilayer films	26
2.4	Cu _{0.88} Mn _{0.12} $M_{FC} - M_{ZFC}$ for 4.5, 9, and 20 nm multilayer films	27
2.5	Cu _{0.88} Mn _{0.12} TRM for a 4.5 nm multilayer film from the IUP magnetometer	28
2.6	Cu _{0.88} Mn _{0.12} maximum activation energies for the three film thicknesses. These measurements fit well to power law dynamics with $c_1 = 1.5 \pm 0.2$ and $c_2 = 0.104 \pm 0.003$. Adjusting the parameters in the droplet model to predict the correct value of the activation energy for the 9 nm film produces an unobserved large spread for the remaining two film widths.	29
3.1	CuMn 4.5 nm 20 G 16 K. The difference in point to point fluctuations between the sample transport and stationary sample method is stark.	34
3.2	CuMn 4.5 nm 20 G 16 K. A blown up view of the point to point fluctuations of the stationary sample IUP SQUID	35
3.3	Experimental Protocol: 1. Cool down in a magnetic field 2. With magnetic field still on, wait at the measuring temperature, T_m for the waiting time, t_w 3. Turn the magnetic field off and measure for the measuring time, t_m 4. With the magnetic field still off, raise the temperature well above the bulk glass temperature, T_g , lower the temperature back to T_m and take a final magnetization measurement. Our experiment is tared to this final magnetization measurement.	37

3.4	Cross section of the head of the magnetometer	40
3.5	Thermal Conductivity of Sapphire	44
3.6	Temperature Control for $16.6000 \text{ K} \pm 0.6 \text{ mK}$, $19.4000 \text{ K} \pm 0.8\text{mK}$, and $24.8000 \text{ K} \pm 1.1 \text{ mK}$. Note how the control improves at lower temperatures where less heat is needed.	46
3.7	Quantum Design dc SQUID circuit	47
3.8	Bare SQUID signal, $1 \Phi_o/V$, on a 1 kHz filter with pickup coil terminals shunted	49
3.9	Current to Magnetic Field calibration performed with Gaussmeter resulting in 0.006 A/G	51
3.10	Simultaneous Readout from both SQUIDs one measuring the sample plus background fluctuations while the second only reads background fluctuations. Note the slight drifts found in the both SQUIDs.	52
3.11	CuMn 4.5 nm 10 G 23 K. This measurement provided our initial calibration for SQUID B subtraction from the sample signal in SQUID A.	53
3.12	CuMn 4.5 nm 20 G 18 K	54
3.13	CuMn 4.5 nm 20 G 20 K	55
3.14	CuMn 4.5 nm 10 G 23 K corrected with SQUID B. Note that this is the same data set found in Figure 3.11.	56
4.1	$\text{Cu}_{0.88}\text{Mn}_{0.12}$, $T_f = 25 \text{ K}$, Irreversible Magnetization in 40 G	58
4.2	Bulk $\text{Cu}_{0.97}\text{Mn}_{0.03}$, $T_g = 25.6 \text{ K}$, Irreversible Magnetization in 20 G. This measurement was taken as a series of short measurement times, 100s, TRMs at various temperatures and should only be used as a rough guide to what the irreversible magnetization should be.	59
4.3	$\text{Cu}_{0.88}\text{Mn}_{0.12}$ TRM decays on a logarithmic scale	61
4.4	74
4.5	$\text{Cu}_{0.97}\text{Mn}_{0.03}$, $T_g = 25.6 \text{ K}$, Waiting Time Experiments	75
4.6	$\text{Cu}_{0.97}\text{Mn}_{0.03}$, $T_g = 25.6 \text{ K}$, Waiting Time Experiments	76
4.7	$\text{Cu}_{0.97}\text{Mn}_{0.03}$, $T_g = 25.6 \text{ K}$, Waiting Time Experiments	77
4.8	$\text{Cu}_{0.97}\text{Mn}_{0.03}$, $T_g = 25.6 \text{ K}$, Waiting Time Experiments	78
4.9	$\text{Cu}_{0.97}\text{Mn}_{0.03}$, $T_g = 25.6 \text{ K}$, Waiting Time Experiments	79
4.10	$\text{Cu}_{0.97}\text{Mn}_{0.03}$, $T_g = 25.6 \text{ K}$, Waiting Time Experiments	80
4.11	$\text{Cu}_{0.97}\text{Mn}_{0.03}$, $T_g = 25.6 \text{ K}$ collection of waiting time effects	81

4.12	Fig. a) and b) show the power law nature of the correlation length growth. In Fig. a) and b), the dashed line represents the crystallite size and the film width respectively.	82
4.13	$f(\tau) = \frac{t}{\tau} e^{-t/\tau}$ for various values of t . For small t , the function is sharply peaked around t and will represent the distribution of relaxation times, $g(\tau)$, in the decay well. The curve at later times, being much more broadly peaked, will incorporate a large range of τ 's at a single point, $g(t)$, and not represent $g(\tau)$ as well. However, the peak of the $S(t)$ and the maximum of $g(\tau)$ remain valid measures of one another.	83
4.14	Effective Phase Diagram of CuMn 4.5 nm	84
4.15	Cu _{0.97} Mn _{0.03} X-ray Diffraction. The FWHM is approximately 0.15 degrees.	84

Chapter 1

Introduction

A spin glass is the low temperature phase of a frustrated, random magnetic system. Through its use as a model glassy system, its study has enriched our understanding of real glasses, statistical mechanics, magnetic ordered states, complex systems, and neural networks, to name a few examples. A number of issues raised by the study of spin glasses and pertinent to these other examples such as finite size effects, lower critical dimensions, and the process of aging will be discussed in this work.

The spin glass phase lacks long range order, such is found in ferro- and anti-ferromagnetic systems, yet possesses randomly oriented magnetic moments which are ‘frozen-in’ over a broad range of relaxation times. In the paramagnetic phase, the individual spins oscillate at a microscopic attempt rate of approximately 10^{12} Hz uncorrelated with one another. As the temperature is lowered, larger clusters of spins begin to oscillate together coherently. The glass temperature in the bulk is defined by the temperature at which the size of these clusters diverge and the relaxation times become infinite. The similarities to structural glasses, which appear to be ‘frozen in’ liquids, lends itself to the nomenclature.

1.1 Experimental History

Materials that would become known as spin glasses were first manufactured by groups such as Charles Kittel's [1] while searching for the Knight shift and Korringa relaxation behavior in these alloys. These metallic spin glasses, such as CuMn, AuFe, and AuMn, typically have concentrations ranging from 0.05-15%. This concentration regime places spin glasses between the paramagnetic regime for lower concentrations and long range ferro- and anti-ferromagnetic regimes at higher concentrations [2]. Improvements in magnetometry sensitivity allowing the use of relatively small magnetic fields ($\simeq 5$ G) revealed the peak in the dc susceptibility [3] and the spin glass phase [4].

The spin glass phase is an example of collective behavior and needs an interaction mechanism between impurity spins to describe the state. For metallic spin glasses, the conduction electrons play the role of mediator, and through a second order effect known as the Ruderman-Kittel-Kasuya-Yosida (RKKY) interaction, provide an exchange energy between magnetic impurities:

$$J(r) = \frac{J_o \cos(2k_F r + \phi)}{(2k_F r)^3}. \quad (1.1)$$

This mechanism yields both ferro- and anti-ferromagnetic couplings of varying strengths based on the random locations of the magnetic impurities. This is sufficient to create both random and frustrated bonds between spin sites, the two crucial characteristics of the spin glass phase. The $1/r^3$ length dependence of the RKKY interaction in these alloys was demonstrated by the

approximately linear relationship between glass temperature and magnetic impurity concentration [5].

Ruderman and Kittel [6] first derived the form of this interaction and applied it to the problem of anomalous broadening of nuclear magnetic resonance resonance of spin 1/2 nuclei in metals with magnetic impurities. Instead of applying the conduction electrons mediation to the nuclear spins, Kasuya applied it to the angular momentum of atomic electrons to demonstrate that both ferro- and anti-ferromagnetic interactions could be generated [7]. Yosida [8] was responsible for applying the previous theoretical results to the Knight shift experiments on CuMn [1].

Interestingly enough, other magnetic materials besides these dilute magnetic alloys can exhibit spin glass behavior. There are examples of magnetic insulators and semiconductors that are also characterized by randomness and frustration in their magnetic bonds [9]. Their magnetic interactions occur through other mechanisms than the RKKY such as dipolar and superexchange interactions [2].

The spin glass state is most clearly identified experimentally by its dc magnetic susceptibility. In bulk spin glasses, the field cooled magnetization is essentially temperature independent below the glass temperature while the zero field cooled susceptibility resembles the ac magnetic susceptibility. The difference between the field cooled and zero field cooled magnetizations is known as the irreversible component of the magnetization for reasons that will soon be discussed. Heat capacity and resistivity measurements are relatively

Figure 1.1: $\text{Cu}_{0.96}\text{Mn}_{0.04}$ Field Cooled and Zero Field Cooled Magnetization.

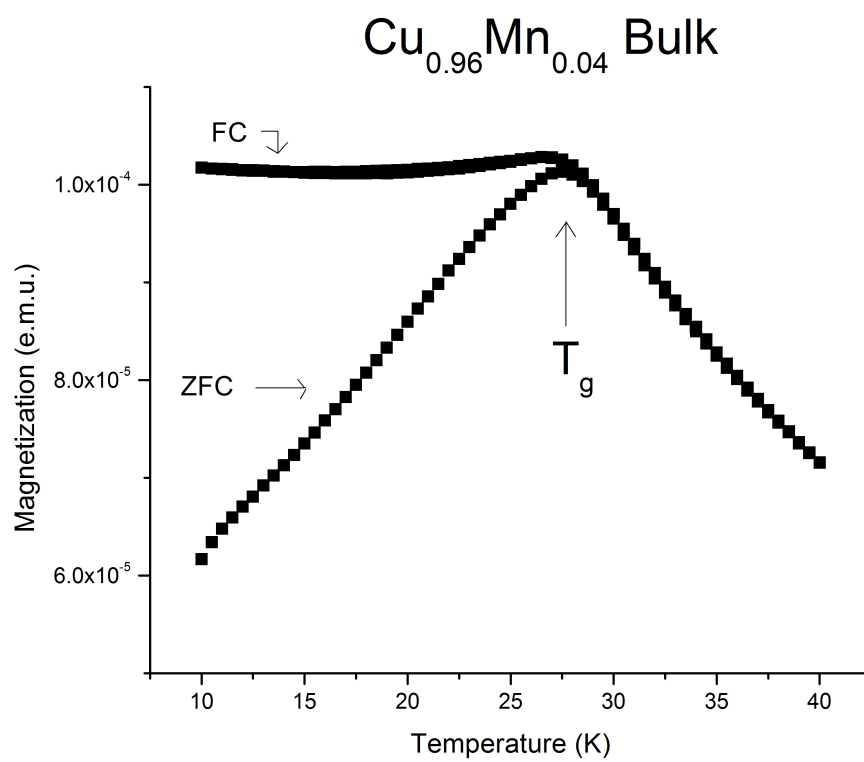
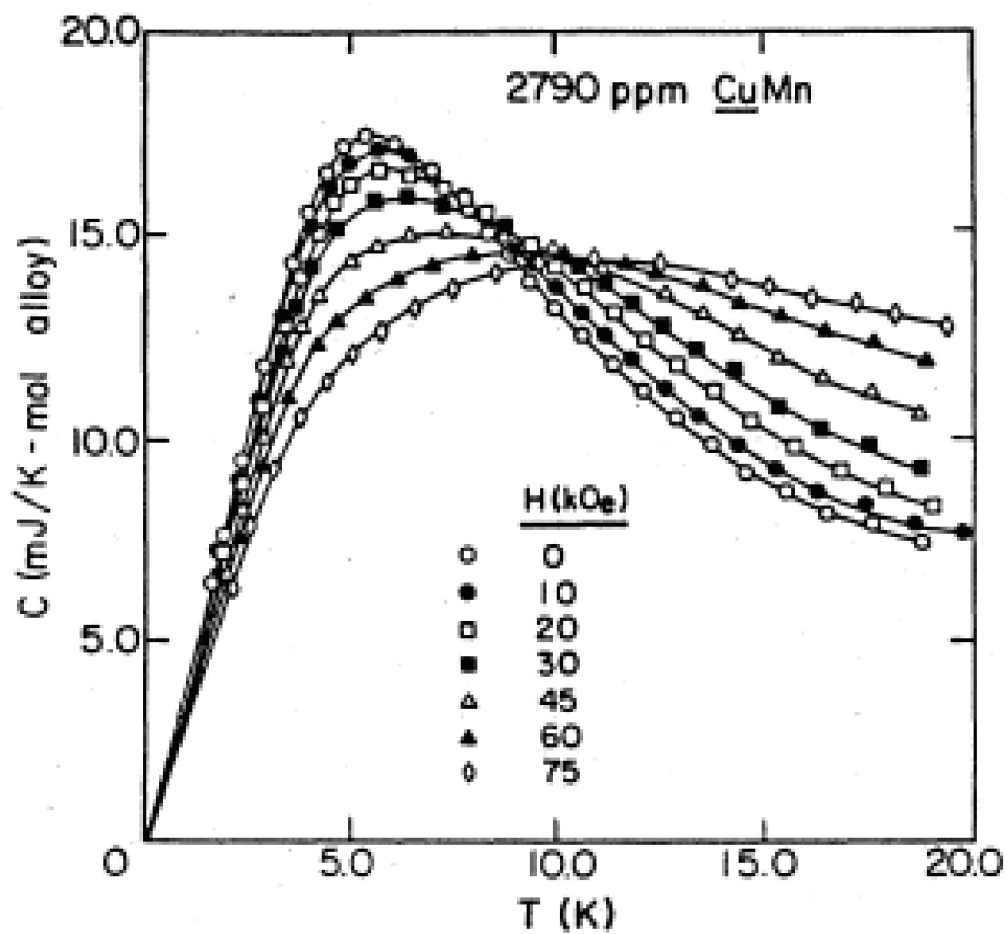


Figure 1.2: $\text{Cu}_{1-x}\text{Mn}_x$ Specific Heat with $T_g = 3 \text{ K}$ [10]

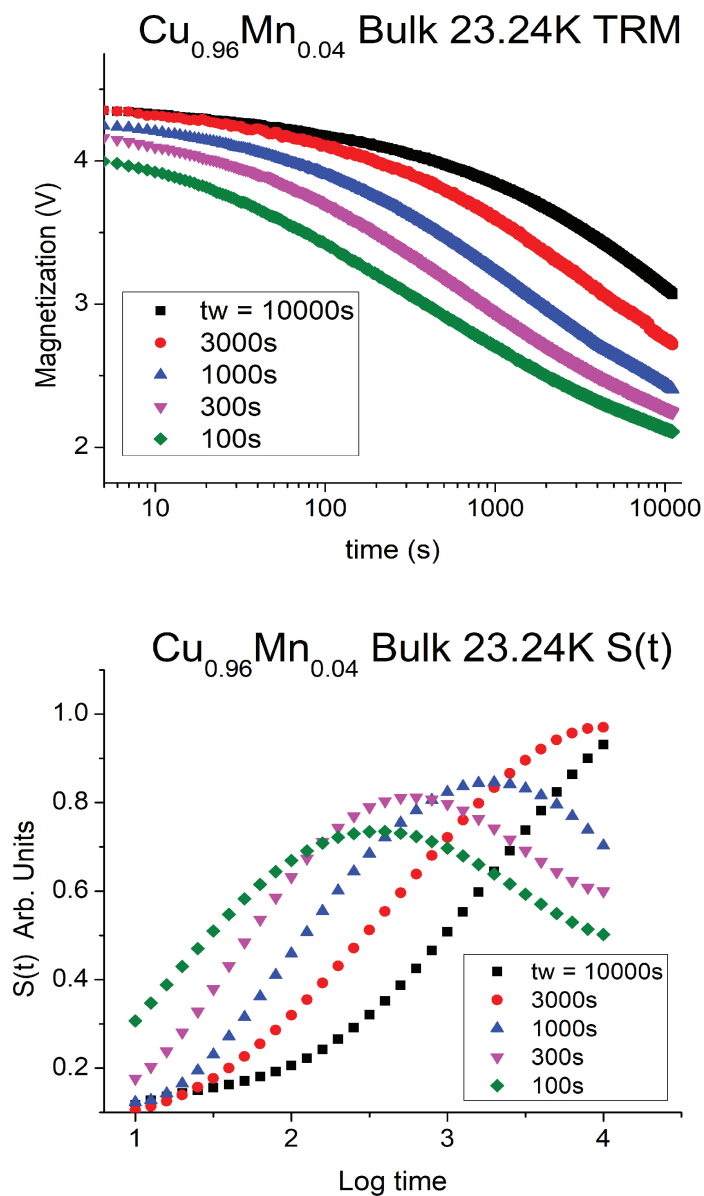


featureless, only exhibiting very broad peaks centered above the glass temperature. This is in stark contrast with other magnetically ordered states such as ferro- and anti-ferromagnets where the specific heat suffers a discontinuity at the ordering temperature.

Another crucial difference between the spin glass phase and the more well understood ferro- and antiferromagnetic states was in the divergence of their magnetic susceptibilities. The FM and AFM phases are characterized by a two spin correlation function and the associated divergence in the linear magnetic susceptibility. The spin glass phase reveals itself through the divergence of higher order derivatives of the free energy with respect to the magnetic induction [11, 12]. This was experimentally verified in the work of Ogielski [13] and Lévy [14].

After the discovery of the shape of the dc field cooled and zero field cooled magnetizations, it soon became clear that neither of the two states were in their equilibrium configuration. The zero field cooled magnetization not only migrates upwards towards the field cooled if the applied magnetic field is left on, but does so in a way that sensitively depends on the waiting time, the time left in its initial state [15]. The waiting time effect, first explored by Struik [16] in polymers, signals that the system in question has a complicated free energy landscape, populated by many free energy minima and a distribution of energy barriers in configuration space. Even more striking, it was shown [17] that the field cooled magnetization, while stationary, was also not an equilibrium state. Upon removing the applied field, the decay of the irreversible part of

Figure 1.3: $\text{Cu}_{0.96}\text{Mn}_{0.04}$ $T_m = 23.4$ K. The $S(t) = \frac{\partial M(t, t_w, T)}{\partial \ln(t)}$ tracks the inflection point of the TRM on a logarithmic time scale.



the magnetization also demonstrated a waiting time effect.

1.2 Theoretical Developments

The divergently long relaxation times, yet complete absence of any periodic spatial ordering, found in the spin glass phase presented a formidable task for researchers attempting to describe these systems. In all previous successful descriptions of ordered many-body condensed matter systems, an order parameter describing a spatial order is postulated and the diverging relaxation time is implied in the infinite sample size limit. This discrepancy between spatial and temporal ordering was one of the first clues that spin glass systems were non-ergodic and not in thermal equilibrium [18].

Real theoretical progress on the spin glass problem began with the work of Edwards and Anderson [19]. Appealing to an analogy with polymer physics, they introduced a novel order parameter devoid of any spatial structure,

$$q_{EA} = \lim_{t \rightarrow \infty} \frac{1}{N} \sum_i^N \langle S_i(0) S_i(t) \rangle. \quad (1.2)$$

The brackets denote a thermal average. The Edwards Anderson model was able to qualitatively reproduce the cusp and zero field cooled magnetization of the spin glass phase.

A mean field long range description of the spin glass phase was provided by the work of Sherrington and Kirkpatrick [20]. They were able to reproduce the cusp in the magnetic susceptibility as well as account for the rounding of the cusp in the presence of strong magnetic fields. Strangely enough, both the

EA and SK models predict cusps in the specific heat which are not found in experiments.

When evaluating models with random couplings between spins, or any random frozen-in disorder, it is necessary to average over a probability distribution of coupling strengths when evaluating the free energy. Averaging the free energy over random couplings, described by a probability distribution function, rather than the partition function, implies we are describing a system with quenched-in disorder as opposed to an annealed system. The free energy, that is proportional to the natural logarithm of the partition function, is difficult mathematically to average, or integrate over. When performing averages over couplings, the replica description is employed, where the logarithm is replaced by raising the partition function to the power n .

$$\ln Z = \lim_{n \rightarrow 0} \frac{1}{n} (Z^n - 1) \quad (1.3)$$

This formal maneuver allows us to introduce an Edwards-Anderson-like overlap between possible realizations, or replicas, of our disordered system.

$$q^{ab} = \sum_{i=1}^n \langle S_i^a S_i^b \rangle \quad (1.4)$$

The Sherrington Kirkpatrick solution, without justification, assumed this overlap to be equal for all replicas, $q^{ab} = q$ for every replica a and b . While greatly simplifying the evaluation of the partition function, it introduced pathologies such as a negative zero temperature entropy.

Parisi, in a series of papers [21–23], proposed and outlined a ‘replica symmetry breaking’ scheme where the various q^{ab} between replicas took on

nontrivial values. The order parameter in this final formulism is $P(q)$ where P describes the probability that two replicas will have overlap q . Mezard, Virasoro, and others further outlined the ramifications of replica symmetry breaking in terms of an ultrametric space organization of replica ground states [24][25].

This novel solution was at odds with the existing understanding of ordered states. In the traditional paradigm, only one unique ground state exists, and the low temperature properties such as specific heat and susceptibilities are determined by low energy, long wavelength excitations above the ground state. In the replica breaking scheme, the properties of the system are determined rather by thermally activated fluctuations across a broad distribution of energy barriers between different unique ground states.

A separate model, generally referred to as the droplet model, was proposed by Fisher and Huse [26–28]. In their picture, the spin glass phase, while still lacking in any long range periodic order, possessed a unique ground state and 'droplet' like domains act as the low energy excitations. Despite their fundamental disparities, it has been difficult experimentally to distinguish between the two theories. Both models predict a broad distribution of activation energies, similar decays of the irreversible component of the magnetization, and temperature cycling properties [29].

The differences between the pictures only emerge out of their subtle respective quantitative predictions. While activation energies in both theories scale with the spin glass correlation length, our initial investigation into the

properties of CuMn thin films revealed that the energy barriers scale according to the replica symmetry breaking scheme as opposed to the droplet model [30]. Additionally, previous measurements on $1/f$ noise in spin glasses seem to indicate a hierarchical structure of ground states [31, 32]. There is still discussion on which model is relevant to real spin glass systems, but most experiments indicate a nontrivial organization of ground states.

Numerical simulation has played an outsized role in understanding the spin glass phase. Many of the usual probes of ordered states in magnetic materials such as neutron scattering fail to reveal domain structures in spin glasses. Parisi's, as well as Sherrington and Kirkpatrick's solution, being infinite dimensional, i.e. every magnetic site couples to one another regardless of site location, lack domains and their related correlation lengths. Correlation lengths only emerge when short range interactions are considered, yet are difficult to determine in real spin glass systems. The power of numerical studies is in their ability to ascertain domain growth by observing the individual spin site states.

Reiger and his collaborators, in particular, greatly advanced this field in his numerical studies of the spin glass state [33]. Motivated by the replica method, as well as the fact that the nonlinear magnetic susceptibility diverged, they considered the four point correlation function,

$$G_T(r, t_w) = \frac{1}{N} \sum_{i=1}^N \frac{1}{t_w} \int_{t_w}^{2t_w} dt [\langle S_i^a(t) S_{i+r}^a(t) S_i^b(t) S_{i+r}^b(t) \rangle]_{av}. \quad (1.5)$$

This correlation function contains the overlap of two spins separated by a dis-

tance for two separate replicas, then averaged over a large number of replicas. Recall that the usual two point correlation function, $G_T(r) \sim \langle S_i S_{i+r} \rangle$, which becomes nontrivial in spatially ordered systems such as ferro and antiferromagnets, remains zero in the spin glass phase. Integrating the correlation function over distance between spin sites yields the correlation length,

$$\xi(t_w) = 2 \int_0^\infty G_T(r, t_w) dr. \quad (1.6)$$

This is motivated by the quasi-exponential form of $G_T \sim e^{-r/\xi}$ which integrates to ξ . Reiger's result was that the correlation length grew as

$$\xi \sim t^{\alpha(T)}. \quad (1.7)$$

It is important to note that this is at odds with the droplet model which predicts a logarithmic growth of domains, $\xi \sim (T \ln t)^\psi$.

Numerical simulation has also proved essential in determining the lower critical dimension of the spin glass phase. The lower critical dimension (LCD) is the lowest dimension for which the system will undergo a phase transition at a non-zero temperature. All evidence points to the LCD being between two and three. This is determined by multiple simulations matching domain size and corresponding relaxation times

$$\tau(T) \sim |T - T_c|^{-z\nu} \sim \xi^z \quad (1.8)$$

in two [34] and three dimensions [35]. This work has been more recently confirmed for larger sample sizes [36–38] as well as supported analytically [39].

Our study of the spin glass phase combines elements of the lower critical dimension, correlation length growth and their associated energy barriers, and the finite thickness of our samples. In lieu of the usual probe of ordered magnetic states, the study utilizes the width of our CuMn films.

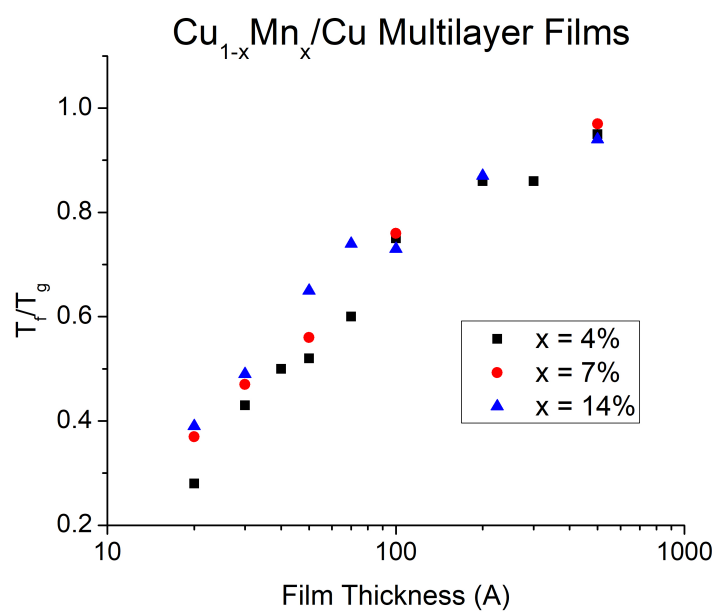
1.2.1 Previous Work on Spin Glass Thin Films

The fact that the lower critical dimension of the spin glass phase is less than three makes thin films of these materials an inviting probe of the spin glass state. Below its lower critical dimension, a system inherits a zero temperature phase transition. The question of how the broad range of relaxation times in the spin glass phase is affected is therefore a pertinent one and directly addressed in our waiting time experiments.

One of the first experimental studies of two dimensional spin glasses was performed on $\text{Cu}_{1-x}\text{Mn}_x$ multilayers by Kenning [46, 47]. By measuring the field cooled and zero field cooled dc susceptibility of films of various thickness, the authors were able to establish that the freezing temperature, T_f , decreased with the film thicknesses [48].

A host of experiments on films of various spin glass materials [49–51] confirm a gradual crossover from three dimensions with a finite temperature phase transition at the bulk glass temperature, to two dimensions with a zero temperature phase transition. In the thermodynamic limit, in three dimensional systems, the maximum energy barrier diverges at the glass temperature. These experiments with various film thicknesses suggest that the upper end

Figure 1.4: Freezing Temperatures of various concentrations and film thicknesses of $\text{Cu}_{1-x}\text{Mn}_x$ [47]



of the distribution of energy barriers is cut off by the finite film thickness. The thinner the film, the more of the distribution is cut off and the apparent glass temperature, which will be henceforth referred to as the freezing temperature, is further reduced. Sandlund [52] in particular was able to illustrate the apparent nature of the freezing temperature by demonstrating its time dependence. As the measurement time, or cooling rate, was increased in dc measurements, or correspondingly, the frequency was decreased in ac measurements, the freezing temperature appreciably decreased.

The ideas of the correlation length growth, found in simulations, finite film thickness, cut off relaxation time distributions, and reduced freezing temperatures first came together in the work of Guchhait [53]. Combining the correlation length growth,

$$\xi(t, T) = c_1 a_o \left(\frac{t}{\tau_o}\right)^{c_2 T/T_g}, \quad (1.9)$$

with the Arrhenius Law,

$$t = \tau_o e^{\Delta/T}, \quad (1.10)$$

yields an expression connecting the maximum activation energy associated with a domain size ξ of correlated spins [54].

$$\frac{\Delta_{max}}{k_B T_g} = \frac{1}{c_2} \left[\ln\left(\frac{\xi(t, T)}{a_o}\right) - \ln c_1 \right] \quad (1.11)$$

In these expressions, c_1 and c_2 are material dependent constants, Δ represents the activation energy, T_g is the *bulk* glass temperature, $\tau_o \sim \frac{\hbar}{k_B T_g}$ is a microscopic exchange time, and t and T represent the time and temperature respectively.

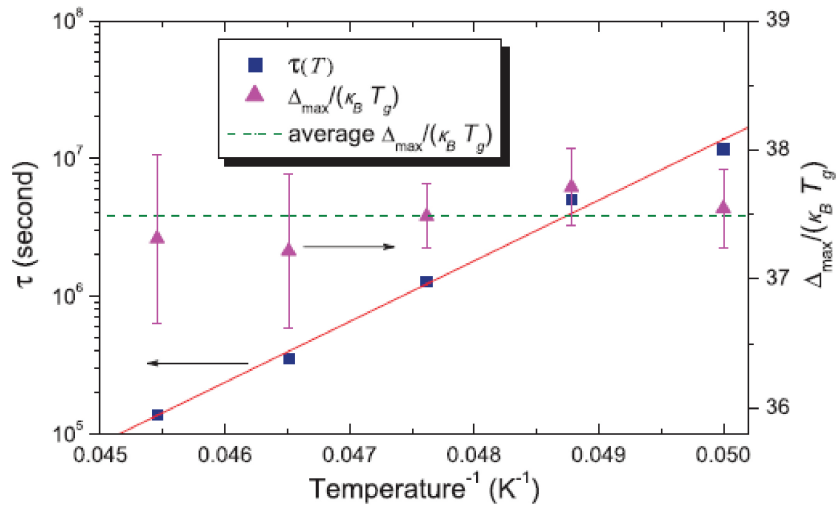
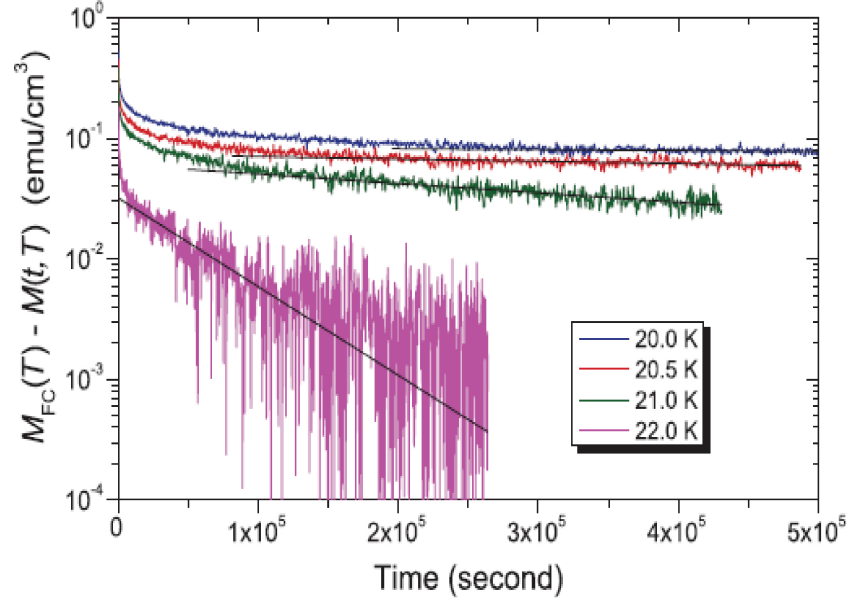
The authors postulate that once the correlated region reaches the film boundaries, it crosses over to a two dimensional spin glass and the correlation length as well as the maximum activation energy cease to grow. The time it takes the correlation length to reach the film thickness is known as the cross-over time, t_{co} . After the cross-over time, the ordered state becomes a collection of domains of the same correlation length all dominated by the same activation energy.

$$\frac{\Delta_{max}}{k_B T_g} = \frac{1}{c_2} \left[\ln\left(\frac{L}{a_o}\right) - \ln c_1 \right] \quad (1.12)$$

It is noteworthy that the maximum activation energy is now independent of time and temperature, provided of course that one has waited until the cross over time.

The first attempt to measure this cross over behavior was performed on the candidate spin glass material, $\text{Ge}_{0.89}\text{Mn}_{0.11}$, by Guchhait [55]. The authors analyzed the long time behavior of the Thermal Remanent Magnetization (TRM), the difference between the field cooled and zero field cooled magnetizations, close to the freezing temperature. If this previously mentioned picture is correct, a typical three dimensional decay, indicative of a broad range of relaxation times, takes place until a temperature dependent cross-over time. After this time, the decay will continue as an exponential decay representing a single relaxation time connected to the film width dependent maximum activation energy. Their experiments displayed cross-over behavior. Decays of the TRM were observed indicating a single relaxation time over a range of temperatures, but suffered from two main issues. One, they only had one film

Figure 1.5: $M_{FC} - M_{ZFC}$ in $\text{Ge}_{0.89}\text{Mn}_{0.11}$ at various temperatures. $T_f = 24$ K



at 15.5 nm film thickness. To truly demonstrate the time dependence of the correlated domains, it is necessary to experiment on different thicknesses of films. Also, GeMn isn't a pure spin glass. It has a ferromagnetic phase and re-entrant spin glass phase. One would hope to see this cross over behavior in a canonical spin glass.

Chapter 2

Glassy Dynamics in Spin Glass Multilayer Thin Films

In order to confront these issues, multilayer samples of three different thicknesses of CuMn/Cu were fabricated. CuMn is a well studied and understood spin glass. Also, by having three different thicknesses, the time dependence of the correlation length can be better explored.

The CuMn/Cu multilayers samples consisted of 40 bilayers of either 4.5, 9.0, or 20 nm of CuMn and 60 nm of Cu. The multilayer samples were dc sputtered at an argon pressure of 2 mTorr. A sputtering rate of approximately 1 Å per minute is utilized. This deposition rate is determined by the use of a calibration sample, also CuMn, whose height is determined, post deposition, by Atomic Force Microscopy. The total width of the films is set by depositing at the known rate. Errors in the width are within 5%. Two different 99.999% CuMn targets were utilized (a set of 4.5-, 9.0-, and 20-nm CuMn multilayers from each) with nominal Mn concentrations of 13.5 at. %. The Cu target was 99.999% Cu.

Two 1- μm thick CuMn films were grown, one from each target, and magnetometry measurements on these bulk samples yielded similar magnetic

properties with a spin-glass temperature T_g of 54 ± 1 K for one target and 52 ± 1 K for the other. For simplicity, we shall take $T_g = 53$ K in what follows. Using the extrapolation of Refs. [35,36], this translates to a Mn concentration of ~ 11.7 at. %.

The experimental data on the multilayers were obtained in two laboratories. The measurements at The University of Texas at Austin were performed on a Quantum Design superconducting quantum interference device (SQUID) magnetometer, while those at Indiana University of Pennsylvania (IUP) were performed on a home-built SQUID magnetometer which will be described in detail in the following chapter. The former measured the time-dependent zero-field-cooled and field-cooled magnetizations, $M_{ZFC}(t, T)$ and $M_{FC}(t, T)$, while the latter measured the thermoremanent magnetization $M_{TRM}(t, T)$. These three quantities are related by

$$M_{ZFC}(t, T) + M_{TRM}(t, T) = M_{FC}(t, T). \quad (2.1)$$

In both laboratories, the CuMn mesoscale multilayer samples were quenched from a temperature of ~ 90 K to a measurement temperature $T_m < T_f$ at a rate of ~ 10 K/min.

In the thin films of $\text{Cu}_{0.88}\text{Mn}_{0.12}$, it was found that the M_{FC} possesses a time dependence. This is in contrast to the corresponding behavior in bulk spin glasses where the M_{FC} is essentially time independent. This behavior can be interpreted as a manifestation of the apparent, time dependent, nature of the three dimensional spin glass freezing temperature. As opposed to the

three dimensional behavior where the M_{ZFC} decays towards the stationary M_{FC} , now both quantities are decaying towards the extrapolated low temperature Curie-Weiss value. This discrepancy becomes important when analyzing dynamical magnetic measurements.

Because $M_{FC}(t, T)$ changes with time, when the magnetic field is applied, some small magnetization arises from states that transition before magnetization measurements can be made. This time-varying magnetization must be subtracted from the measured time-dependent difference in magnetizations, $M_{FC}(t, T) - M_{ZFC}(t, T)$, to obtain the true measured irreversible magnetization. The manner in which this is accomplished is to measure the ratio $M_{ZFC}(t, T)/M_{FC}(t, T) = \alpha(t)$ as a function of time t until it reaches a final constant value α_f to within measurement error bars. For $\alpha_f = 1$, this would signify that $M_{ZFC}(t, T)$ has reached the field-cooled value for the magnetization $M_{FC}(t, T)$. However, because of the time interval for which the measurement of $M_{ZFC}(t, T)$ is blind, $\alpha_f < 1$, requiring a subtraction of the contribution to $M_{FC}(t, T)$ that occurred during that time interval. This is accomplished by subtracting an amount $\epsilon = 1 - \alpha_f$ from the measured $M_{FC}(t, T)$. The irreversible magnetization, $(1 - \epsilon)M_{FC}(t, T) - M_{ZFC}(t, T)$, then approaches zero in the long-time limit. Typically, ϵ is found to be small, on the order of 0.005. Validation of this reasoning was found by comparing similar results in the activation energies found in the M_{TRM} measured on the home built SQUID magnetometer at IUP.

The activation energies are determined fitting the post cross over, long

Figure 2.1: $\text{Cu}_{0.88}\text{Mn}_{0.12}$ FC-ZFC for 4.5, 9, and 20 nm multilayer films

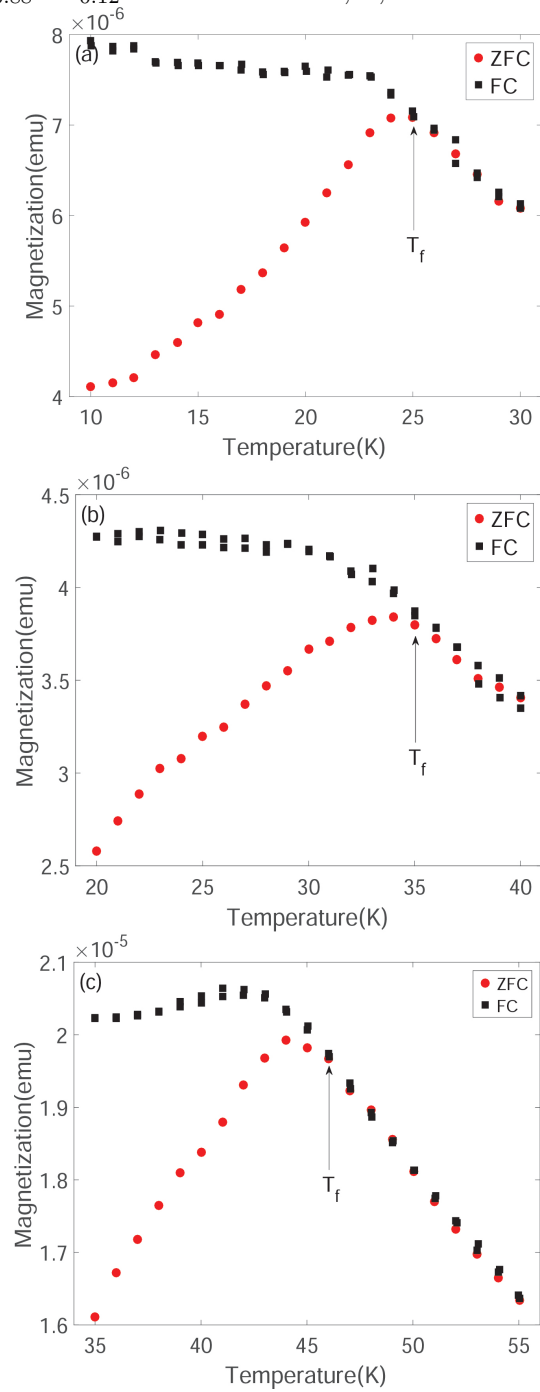


Figure 2.2: $\text{Cu}_{0.88}\text{Mn}_{0.12}$ FC-ZFC for 4.5, 9, and 20 nm multilayer films

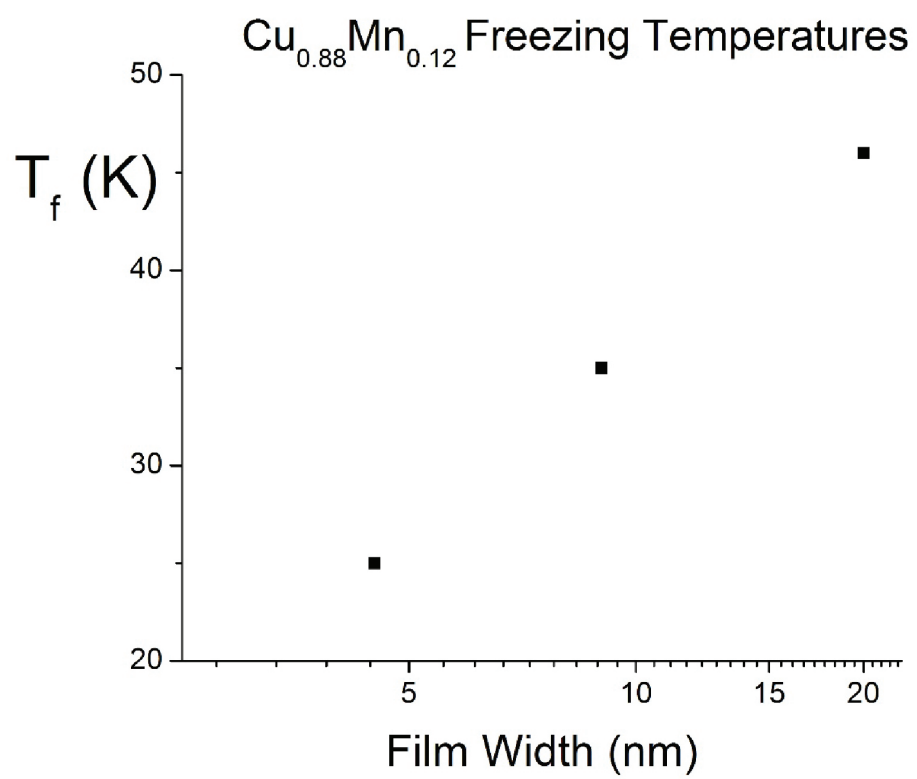


Table 2.1: $\Delta_{\max}(\mathcal{L})/k_B$ extracted at different temperatures for each multilayer CuMn thin film.

\mathcal{L}	T_f	T_m	$\Delta_{\max}(\mathcal{L})/k_B$
4.5nm	25K	22.5K	907±2K
		23K	910±7K
		23.5K	904±2K
9nm	35K	31K	1243±8K
		31.5K	1243±13K
		32K	1252±10K
20nm	46K	41K	1648±4K
		41.5K	1650±2K
		42K	1652±8K

time $M_{TRM}(t, T)$ behavior to an exponential decay. The time constant of the decay can then be related to an activation energy via the Arrhenius Law. This measurement is, of course, independent of the model, either Droplet or the Hierarchical, but determining when the temperature dependent cross over time occurs is often not obvious from the shape of the decay. It must be determined in a self consistent way with considerations of the form of the correlation length growth, the relationship between correlation length and activation energy, both model dependent, as well as the freezing temperatures for the different films.

Within the considerations of the hierarchical model, we expect a logarithmic dependence between the freezing temperature and film thickness.

$$\frac{T_f}{T_g} c_2 \ln\left(\frac{t_{co}}{\tau_o}\right) + \ln c_1 = \ln\left(\frac{L}{a_o}\right) \quad (2.2)$$

This relationship is well respected by our three film thicknesses and yields

values of $c_1 = 1.448$ and $c_2 = 0.104$ for experimentally reasonable cool down and measurement times for t_{co} , $t(4.5\text{nm}) \sim 2,200$ s, $t(9\text{nm}) \sim 600$ s, and $t(20\text{nm}) \sim 470$ s. Using these values of c_1 and c_2 it is possible to predict crossover times for lower temperatures.

$$t_{co} = \left(\frac{L}{a_o c_1}\right)^{\frac{T_g}{c_2 T}} \quad (2.3)$$

These crossover times represent the time it takes for the correlation length to reach the film thickness. After waiting for these times, the spatial growth of the correlations ceases and the remaining M_{TRM} decays can be fit to a single time constant exponential decay. This time constant is then related to the maximum activation energy via the Arrhenius Law. The direct connection between film thickness and maximum activation energy,

$$\frac{\Delta_{max}}{k_B T_g} = \frac{1}{c_2} [\ln(L/a_o) - \ln c_1], \quad (2.4)$$

is displayed in Figure 2.2 and 2.6.

The relationship between maximum activation energies, cross over times, freezing temperatures, film widths, and the constants c_1 and c_2 are not only consistent, but actually over determined by the use of three different film thicknesses. In practice, all these parameters, or results, are determined simultaneously by fitting their values within experimental errors. The fact that it is even possible to do so within the hierarchical picture is a testament to its validity.

A similar analysis cannot be performed within the Droplet Model, where a power law relationship is predicted between the freezing temperature

Figure 2.3: $\text{Cu}_{0.88}\text{Mn}_{0.12}$ FC and ZFC for 4.5, 9, and 20 nm multilayer films

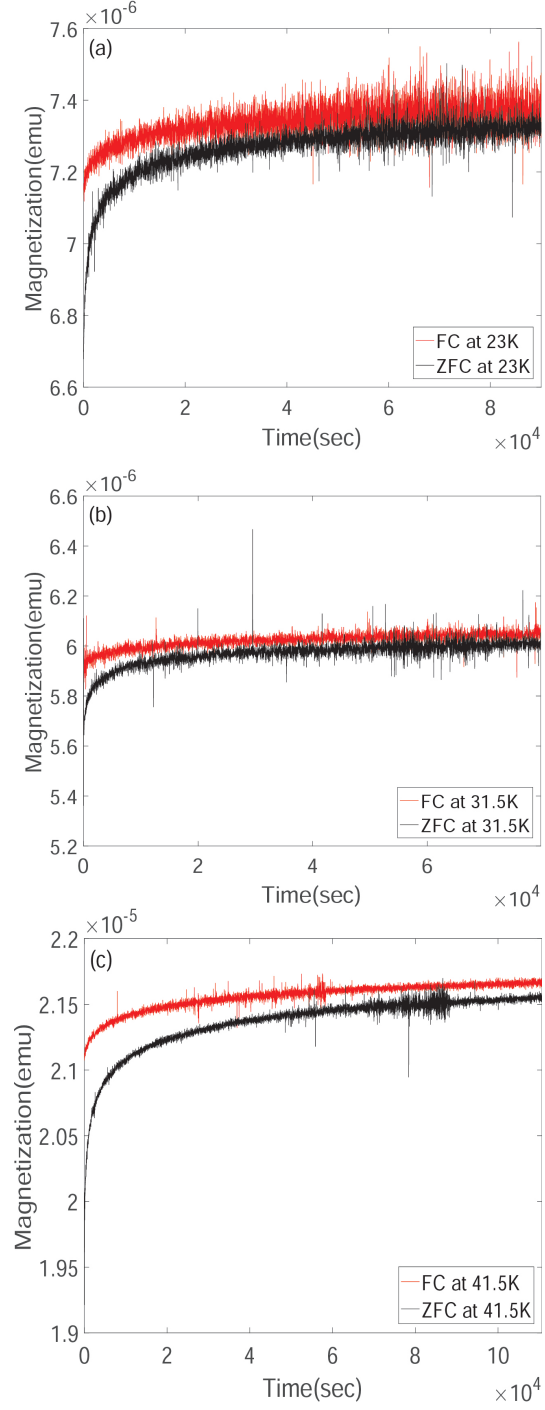


Figure 2.4: $\text{Cu}_{0.88}\text{Mn}_{0.12}$ $M_{FC} - M_{ZFC}$ for 4.5, 9, and 20 nm multilayer films

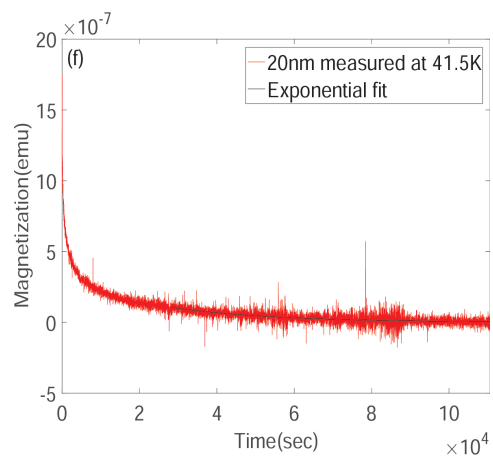
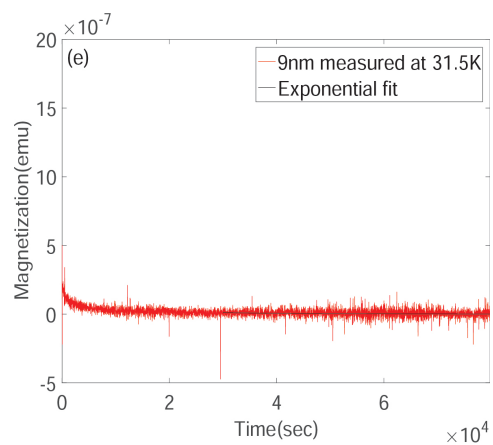
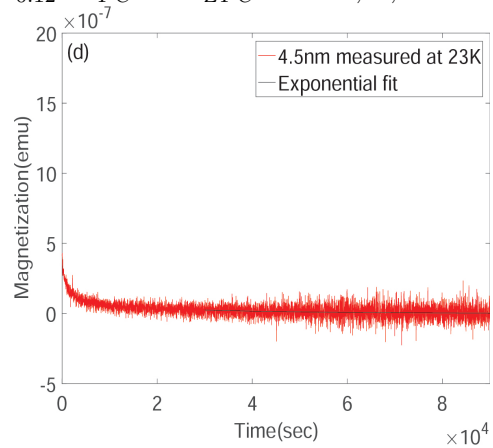


Figure 2.5: $\text{Cu}_{0.88}\text{Mn}_{0.12}$ TRM for a 4.5 nm multilayer film from the IUP magnetometer

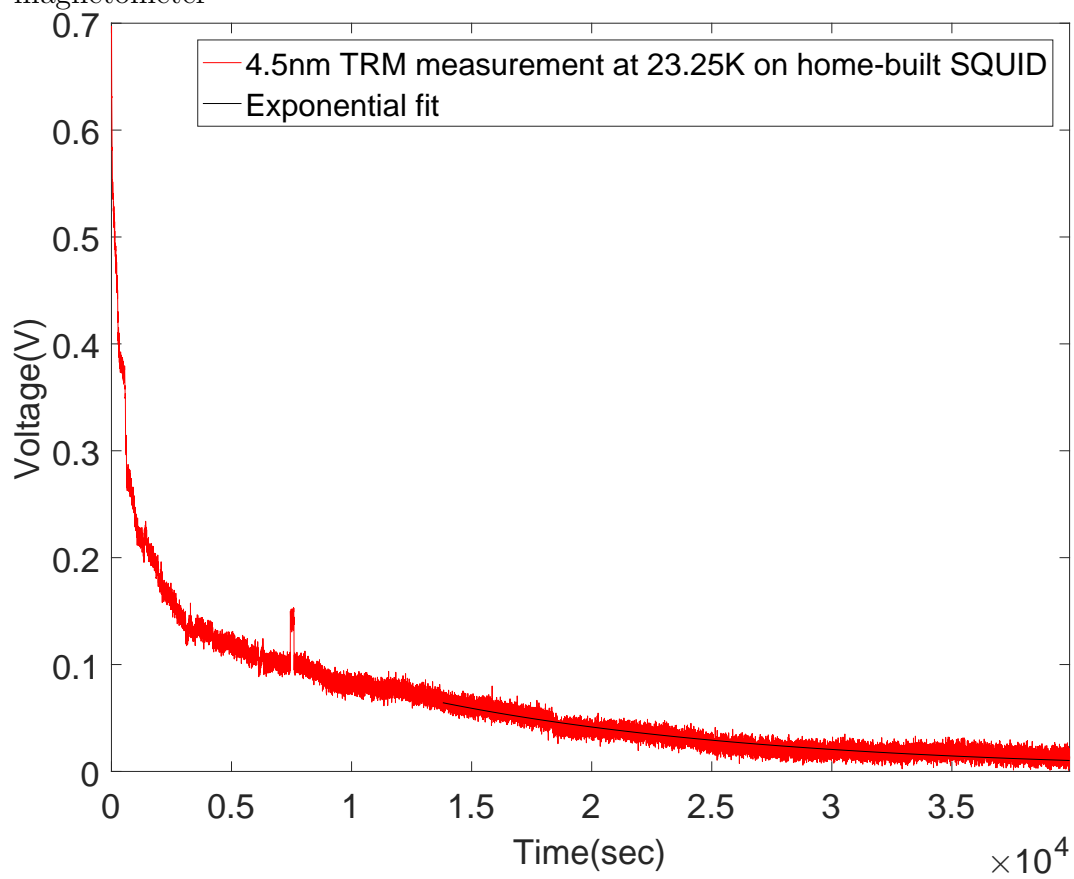
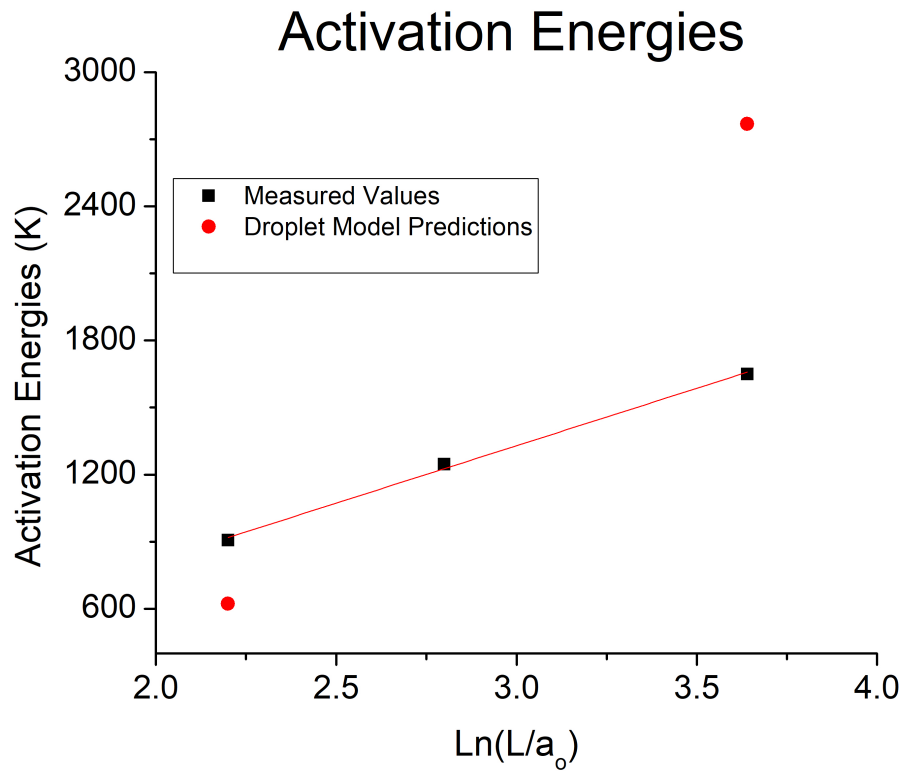


Figure 2.6: $\text{Cu}_{0.88}\text{Mn}_{0.12}$ maximum activation energies for the three film thicknesses. These measurements fit well to power law dynamics with $c_1 = 1.5 \pm 0.2$ and $c_2 = 0.104 \pm 0.003$. Adjusting the parameters in the droplet model to predict the correct value of the activation energy for the 9 nm film produces an unobserved large spread for the remaining two film widths.



and the film thicknesses.

$$\frac{T_f}{T_g} \left[\ln \left(\frac{t(L)}{\tau_o} \right) \right]^{1/(1+\nu_2\psi_2)} = \left(\frac{L}{a_o} \right)^{(\psi_3+\psi_2\nu_2\theta_3)/(1+\psi_2\nu_2)} \quad (2.5)$$

The subscripts refer to the dimensionality of the parameter. There is some discrepancy between simulation and experiment with respect to the values of the parameters. Experimental work by Dekker [50] shows $\psi_2 \simeq 1.0$ and Sandlund [52] shows $\psi_2\nu_2 \simeq 1.6 \pm 0.2$, whereas simulation work by Young [58] yields $\nu_2 \simeq 3.45$. Fisher and Huse [45] analytically show $\theta_3 \simeq 0.2$. Using the simulation values for ν_2 , the T_f for the 9 nm film, and the smallest possible value for $\psi_3 \geq \theta_3 \simeq 0.2$ yields an unphysical value of the cool down and measurement time of 10^{21} s.

On the other hand, using the experimental value for $\nu_2\psi_2$ and a reasonable value of a few hundred seconds for the measurement time yields a reasonable value of $\psi_3 = 0.56$. However, with these same values for the parameters, the measurement time for the 4.5 nm film is $\sim 10^7$ s, much longer than the time scale of our experiment. This unrealistic spread of predicted measurement times is due to the power law nature of the time to film width relationship as opposed to the logarithmic relationship for hierarchical dynamics.

In addition to these discrepancies in the freezing temperatures, there are also issues with interpreting the activation energies in the context of the droplet model. Using a value of $\psi = 1.0$, as found experimentally, and using the value for the activation energy of the 9 nm film, 1250 K, one can see

$\alpha = 0.73$. With these values of ψ and α , one finds a much larger than observed spread of activation energies for the two other film widths, 623 K and 2769 K for the 4.5 nm and 20 nm films respectively.

Even disregarding the previously found values for ψ and α yields contradicting results within the framework of the droplet theory. Taking the measured values for the 4.5 nm and 9.0 nm films, one can fit values of ψ and α yielding 0.53 and 0.043 respectively. With these values, a maximum activation energy of 1942 K is predicted, at odds with the measured value of 1650 K.

Provided one has waited past the crossover time, the activation energies depend solely on the film thickness. Through exploitation of the LCD, it is now possible to 'freeze' the correlation length growth and measure its associated activation energy. This offers a subtle, yet compelling, argument for the relevance of the hierarchical model over the droplet picture.

Chapter 3

Experimental Apparatus

Superconducting Quantum Interference Device (SQUID) magnetometers are the standard apparatus in research laboratories for taking magnetic measurements on samples with minute signals ($\leq 10^{-4}$ e.m.u.). Commercial machines are designed to accommodate a plethora of different measurements such as field cooled-zero field cooled susceptibility, thermoremanent magnetization, and hysteresis measurements [62, 63]. While these commercial machines are extremely versatile and convenient, there have been many home built SQUID magnetometers built to outperform them, in terms of signal to noise ratio, at specific tasks [64–68].

This chapter describes the functionality of a custom built SQUID magnetometer housed at Indiana University of Pennsylvania. The work of Dr. Gregory Kenning, at IUP, and Dr. Raymond Orbach, at the University of Texas, is part of a long standing collaboration between the two whose main goal is obtaining a better understanding of the spin glass state through the use of SQUID magnetometry. As such, I had the benefit of being able to travel in between and work at both institutions.

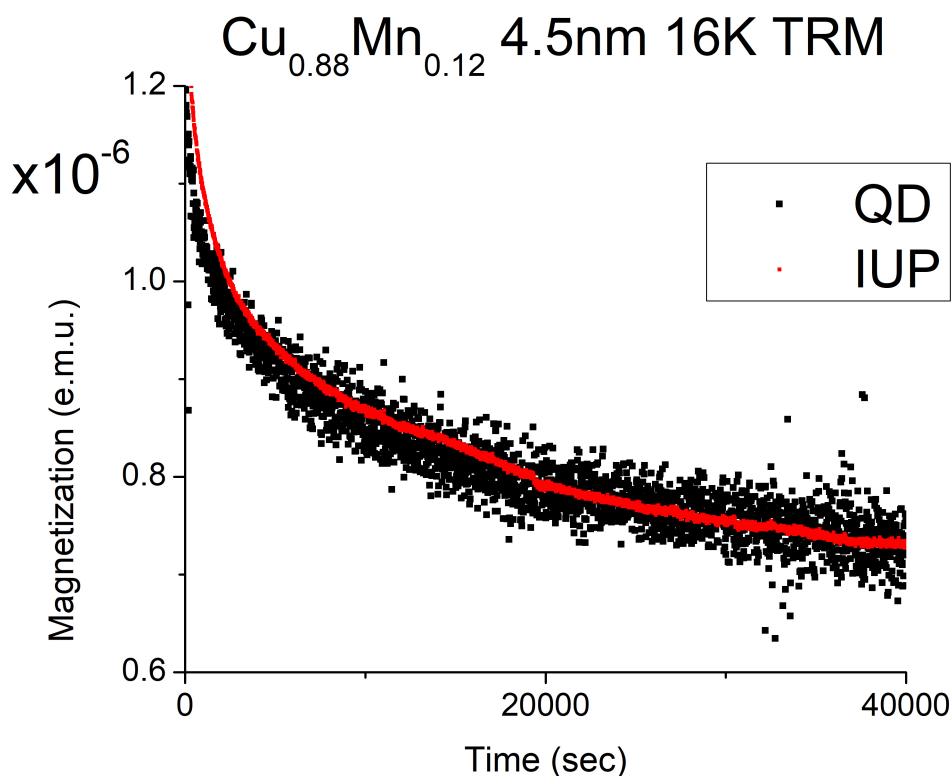
In both commercial and home built machines, two data collection meth-

ods are utilized, sample transport and stationary sample protocols. Both protocols, as well as their advantages and disadvantages, will be described below. One of the main purposes of this chapter is to identify, explain, and discuss solutions to one of the issues plaguing the stationary sample protocol, the presence of low frequency drifts in output voltage [66, 67, 95]. The use of a second SQUID and paired gradiometer pickup coils allows us to separate fluctuations in environment from sample fluctuations aiding the goal of identifying causes of environmental fluctuations with the hope of eliminating them.

In commercial SQUID machines, as well as some home built magnetometers, sample transport in and out of a set of gradiometer pickup coils is utilized. As the magnetic sample is moved through a series of oppositely wound pick up coils over the course of approximately 15 seconds, a SQUID voltage versus position dependence is produced and fit to a standard curve. This determines an averaged net magnetization as well as an error check through bad fits. This method has the advantage of being able to accurately measure magnetic zero as the sample is removed from the coils at the same time that the sample magnetization is being recorded. This eliminates low frequency (less than 0.03 Hz) environmental noise.

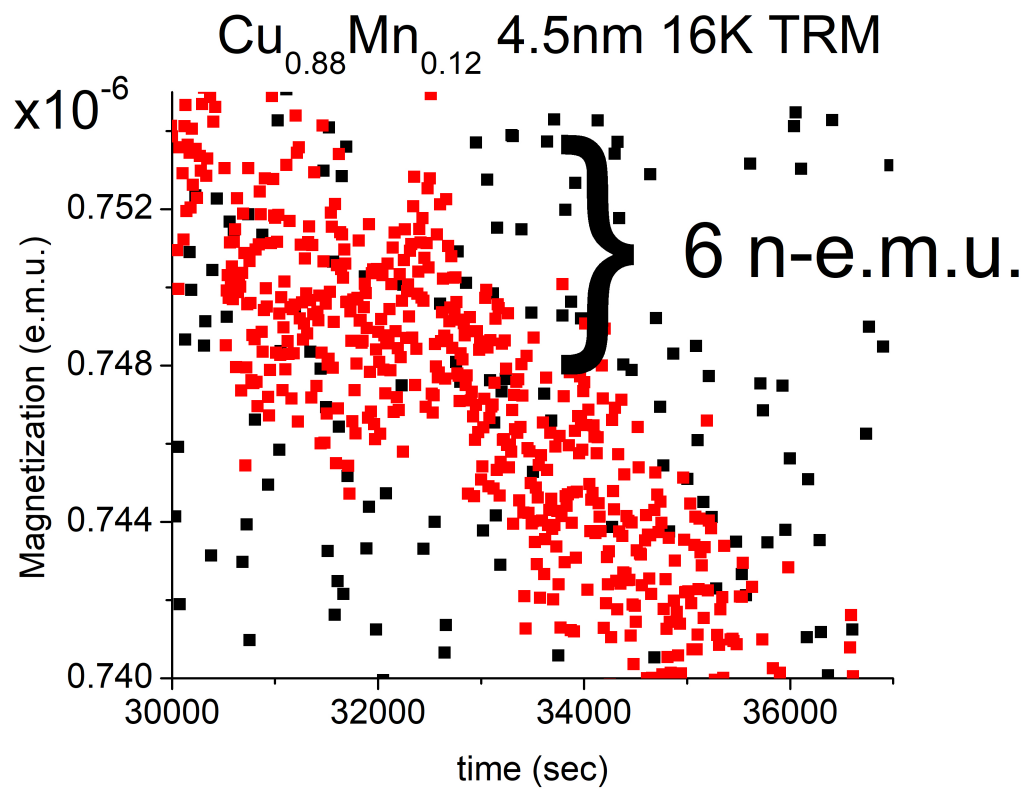
However, through the motion of the sample transport, noise is brought into the data. For minute signals, the width of the point to point fluctuations, greatly increased by motionally induced vibrations is a hindrance to signal resolution. The other popular method of signal acquisition is for the sample to remain stationary. This greatly reduces the amount of vibrational noise in

Figure 3.1: CuMn 4.5 nm 20 G 16 K. The difference in point to point fluctuations between the sample transport and stationary sample method is stark.



terms of point to point fluctuations but introduces low frequency drifts in signal that can be equally destructive to the actual signal. The Quantum Design magnetometer located in Austin, which utilizes a sample transport protocol, possesses a resolution of 27.5 nano-e.m.u., whereas the IUP magnetometer, utilizing a stationary sample measurement protocol, greatly improves on this value with a 1.9 nano-e.m.u. resolution. This improved resolution will make the aging experiments discussed in the following chapter possible.

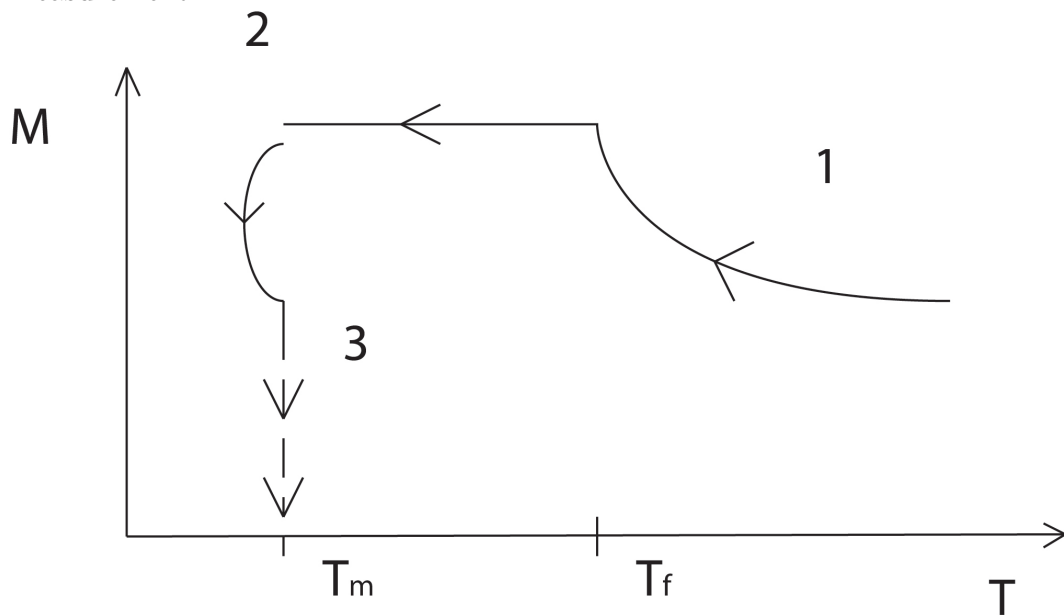
Figure 3.2: CuMn 4.5 nm 20 G 16 K. A blown up view of the point to point fluctuations of the stationary sample IUP SQUID



In the TRM measurements, with measuring times of 10^4 to 10^5 seconds, it becomes obvious through analyzing our data that environmental changes have taken place. In these TRM measurements, true ‘magnetic zero’ is only sampled at the very end of the measuring time. Our protocol starts with the sample at a high temperature, above T_g , and a magnetic field, of 5 to 40 G, is applied. The sample is quenched to the measuring temperature quickly, generally within 30-50 s the temperature has stabilized and is held there, with the field on for the waiting time, t_w , which in our case runs from 100 to 10,000 seconds. After t_w , the magnetic field is cut to zero and the SQUIDS, one with the sample, one without, begin taking data for the duration of the measuring time, t_m . After t_m , with the field still off, the temperature is raised above the T_g , lowered back down to T_m , and once the temperature is stable, one final SQUID measurement is taken. This final data point samples the paramagnetic magnetization of the sample in zero applied field plus whatever contributions are present from the environment. This value is subtracted off from the data taken during t_m leaving us with simply the spin glass TRM with environment contributions removed.

This would leave us with a clean data set if those environmental contributions were constant over the long time scales, approximately a day, of our measurements. Unfortunately, temperature changes, variations in ground voltage, barometric fluctuations, among others, are all environmental factors constantly in flux. What this means for our data is that our last bit of the data during t_m is the most accurate, more immediately compared to ‘magnetic

Figure 3.3: Experimental Protocol: 1. Cool down in a magnetic field 2. With magnetic field still on, wait at the measuring temperature, T_m for the waiting time, t_w 3. Turn the magnetic field off and measure for the measuring time, t_m 4. With the magnetic field still off, raise the temperature well above the bulk glass temperature, T_g , lower the temperature back to T_m and take a final magnetization measurement. Our experiment is tared to this final magnetization measurement.



zero' while the data gets more and more unreliable the farther back in time it's taken.

To the best of our knowledge, this report is the first attempt to isolate one environmental factor from another. After due diligence in electrically (even creating our own ground in addition to installing relays and an isolator-transformer) and magnetically (enclosing the sample/pickup coil/magnetic field coil in superconducting lead) shielding our experiment, we felt confident that electromagnetic noise was not the cause of our low frequency SQUID drifts. This belief was dramatically confirmed when the helium vapor exhaust was blocked and as the pressure increased in the experiment space, the SQUID readout voltage in both SQUIDs steadily increased.

In addition to signal resolution, there are other concerns, namely liquid helium consumption. Commercial SQUIDs and ours have completely different temperature control systems. Quantum Design SQUIDs, for example, allow helium to mist through the sample space which is surrounded by vacuum jackets for temperature control. The pick up coils on the Quantum Design SQUID have to be large enough to surround the insulated sample space, reducing its signal to noise ratio, a concern not shared by the IUP machine. The IUP SQUID design, on the other hand, relies on direct thermal contact to the sample through a low pressure helium gas. This causes approximately twice the rate of helium consumption found in the Quantum Design machine. But, as just mentioned, the IUP machine can be installed with much smaller pick up coils, improving upon its sensitivity.

After describing the structure and functionality of the experimental apparatus, the SQUID readout will be compared with barometric data, taken from the local airport, approximately 5 km from the experiment. Finally, steps taken to decouple atmospheric fluctuations from the experiment space will be described.

3.1 Experimental Apparatus

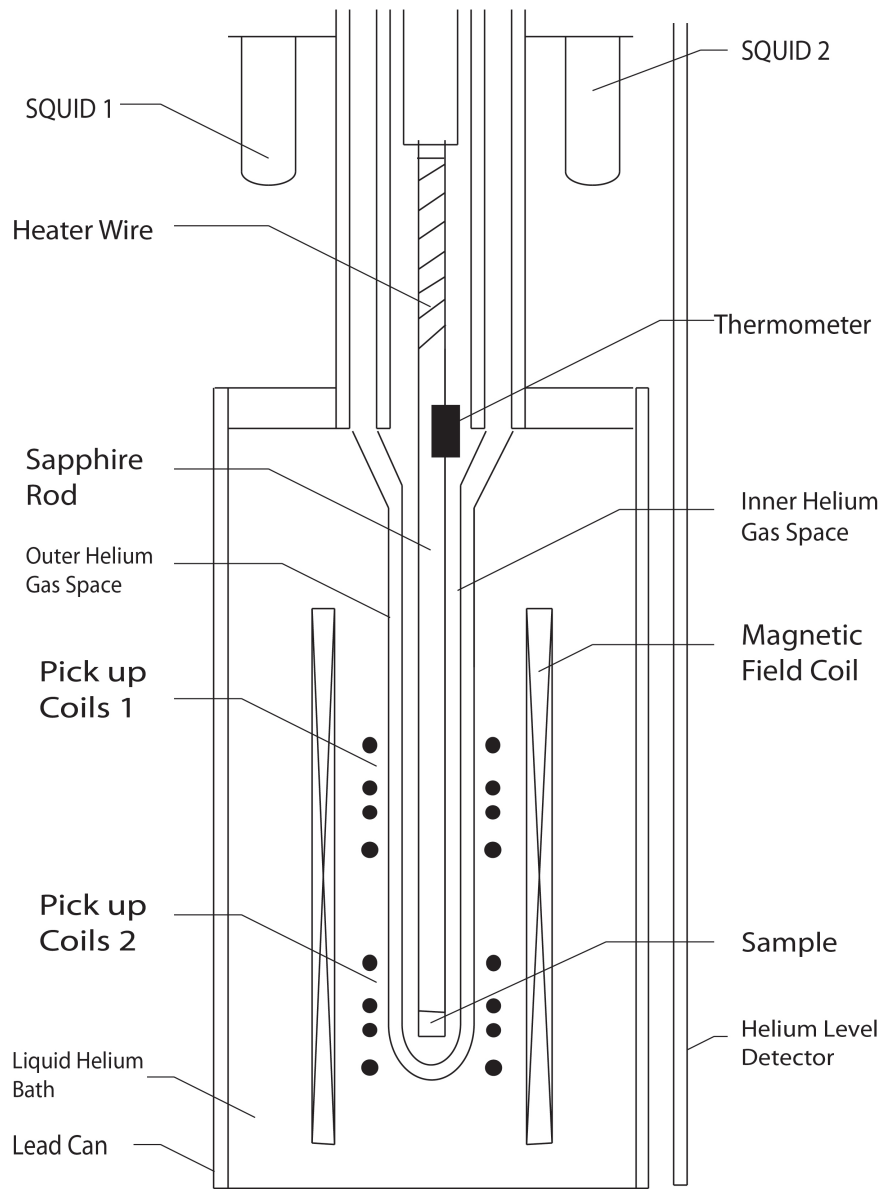
All waiting time experiments, as well as a few activation energy experiments, in this thesis were performed on the custom built dc squid magnetometer located at Indiana University of Pennsylvania. The results from this magnetometer are in volts and calibrated to electromagnetic units by comparison with results obtained on a Quantum Design magnetometer located at the University of Texas at Austin. The magnetometer is roughly based on the design utilized by Joh [71] and Wood [72] for their doctoral work. The initial construction and calibration of the apparatus is found in the Master's thesis of Rost [73].

The apparatus is divided into four main functional components; the chassis, temperature control system, magnet, and SQUID and pickup coil assembly. The head of the magnetometer is illustrated below.

3.1.1 Structure of the Probe

The chassis is an approximately meter long cylindrical structure which sits within a 100 liter helium dewer during operation. The top flange of the

Figure 3.4: Cross section of the head of the magnetometer



probe bolts into the top of the dewer and separates the helium space as well as the sample space from atmosphere. Four stainless steel threaded rods secure the length of the probe from top flange to the bottom lead disc which in turn secures the sample space located below. Five brass helium baffles are spaced evenly between the SQUID space and the top flange. They act to thermally isolate the sample space from the top of the probe at room temperature. The insert, described below, secures the center of the probe.

The electrical controls for the magnetic field, pick up coil heater wire, and liquid helium level gauge are fed through a military grade hermetically sealed electrical connection. Special care was taken to make sure all connections were grounded by insuring the outer metallic mesh is well connected to the socket housing. To further prevent electrical noise from contaminating the SQUID readout, two Tyco Electronics KUP-11D15-12 relays electrically isolate the magnetic field coil and pick up coil heater wire from the probe. The magnetic field and pick up coil heater as well as the relays are powered by Agilent 6611C power supplies. To isolate the helium level detector, the connection is simply disconnected when not filling.

Recent improvements to the helium vapor exhaust system from the liquid helium space have been made. Previously the evaporating helium gas simply exhausted to atmosphere. The exhaust ran through a long thin line to prevent contamination of the helium space by other atmospheric gases. As will be detailed later, fluctuations in barometric pressure proved to have an appreciable impact on the SQUID readouts. The current configuration

allows the helium exhaust to pass through a wide channel to a T-connection. During operation, the T-connection opens to an AliCat Pressure Gauge and Flow Meter which effectively isolates the pressure in the liquid helium space from atmosphere. The output of the flow meter connects to a reservoir which is simultaneously pumped on by an Edwards 18 roughing pump as well as a Leybold Trivac roughing pump. This maintains the reservoir pressure at approximately 25 torr which further prevents back pressure from influencing the liquid helium space pressure. During liquid helium fills, the T-valve can be switched to open to atmosphere.

In addition to the helium exhaust and electric feed throughs, the SQUID line feed throughs have also been improved upon. Upon realizing the importance of barometric fluctuations, it was realized that SQUID line feed throughs, rubber corks, would not be adequate. Specialized bases, which the SQUID preamp bases pressure fit into were designed and installed. The one remaining opening through the top flange is the helium fill port and is capped during operation.

The insert, approximately two meters long, fed through the center of the chassis, is a double chamber stainless steel tube fused to glass at the lower end. The stainless steel concentric tubes are coated in a millimeter thick coating of lead. The outer tube fits snug into the lead circular piece directly above the space housing the SQUIDs. This provides further magnetic shielding to the magnetometer apparatus. Separate pressure valves connect to the inner and outer chambers. Prior to operation, the helium gas pressure in the two

chambers is set to obtain optimal temperature control over the experimental protocol.

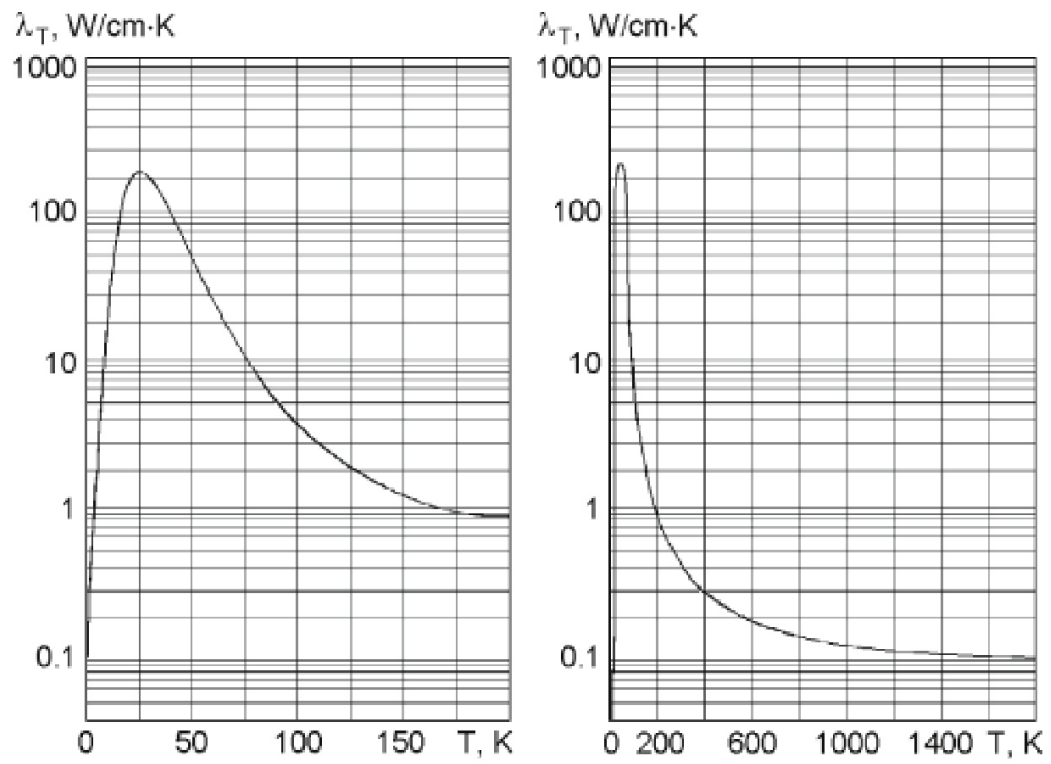
3.1.2 Sample Holder and Temperature Control System

The sample holder is comprised of a long, thin, hollow, 1.5 m stainless steel rod. A 25 cm hollow G10 cylinder separates the steel tube from the sapphire rod at whose end the sample is attached. The top of the stainless steel rod ends in a hermetically sealed electrical feed through. Small 1 mm holes are bored into the stainless steel rod every 10 cm to help ensure a local thermal equilibrium for the wires running through. The two sets of thermometer wire as well as the temperature heater wire runs through this top connection into the sample space. Phosphorous Bronze, non ferromagnetic, twisted wire is used for the thermometers while Manganin AWG 32 is the heater wire. A LakeShore Model 340 Temperature Controller is responsible for reading and maintaining the temperature.

The G10 joining piece plays an important role in heat isolation. Both ends of the G10 piece are separated from their mating piece by Kapton tape, a thermal isolator. A copper rod fits inside the G10 joiner and acts as a heat sink, further isolating the sample space from room temperature.

The sapphire rod is 0.4 cm in diameter and 25 cm in length. Sapphire has exceptionally high thermal conductivity, approximately $100 \text{ W}/(\text{cm K})$, at the experimental temperatures, 15-30 K. The sample is effectively glued to the bottom tip of the sapphire rod with GE varnish.

Figure 3.5: Thermal Conductivity of Sapphire



The wires for the two thermometers as well of the temperature heater wire are run through the stainless steel rod and through the G10 connector. The two thermometers are attached via GE varnish approximately halfway down the sapphire rod. The sample, lower part of the sapphire rod, and thermometers are completely wrapped in teflon tape, effectively trapping the heat contained in the sapphire rod and eliminating temperature gradients along the length of the rod thus ensuring the thermometers record the correct sample temperature. The heater wire is wrapped around the top center of the sapphire rod and affixed with GE varnish. Special care is taken while wrapping it to space the wraps enough so that not too much heat accumulates in one place and burns the wire.

The sapphire rod and sample assembly is located within one of two vacuum chambers. The vacuum chambers are filled with a controllable amount of Helium gas, usually $5 \times 10^{-2} - 3 \times 10^{-1}$ torr, such that the equilibrium temperature rests at 10 to 20 K depending on the needs of the particular experiment.

3.1.3 Squid, Pick up Coil, and Magnet Assembly

Both SQUIDS are Niobium thin film DC SQUIDS, model 50DCSQUID made by Quantum Design. Wire from the SQUIDS run up the chassis to the top plate where they connect to two pre-amps and the signal continues on to a Quantum Design model dc5000 SQUID Controller. Voltage readouts from the control box continue to two Keithley Model 2002 digital voltmeters. The

Figure 3.6: Temperature Control for $16.6000\text{ K} \pm 0.6\text{ mK}$, $19.4000\text{ K} \pm 0.8\text{ mK}$, and $24.8000\text{ K} \pm 1.1\text{ mK}$. Note how the control improves at lower temperatures where less heat is needed.

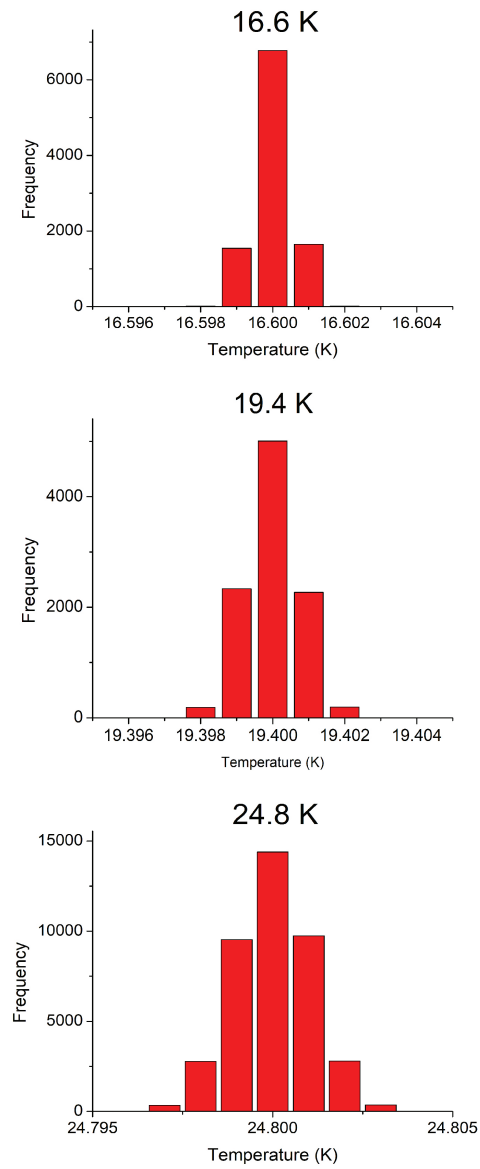
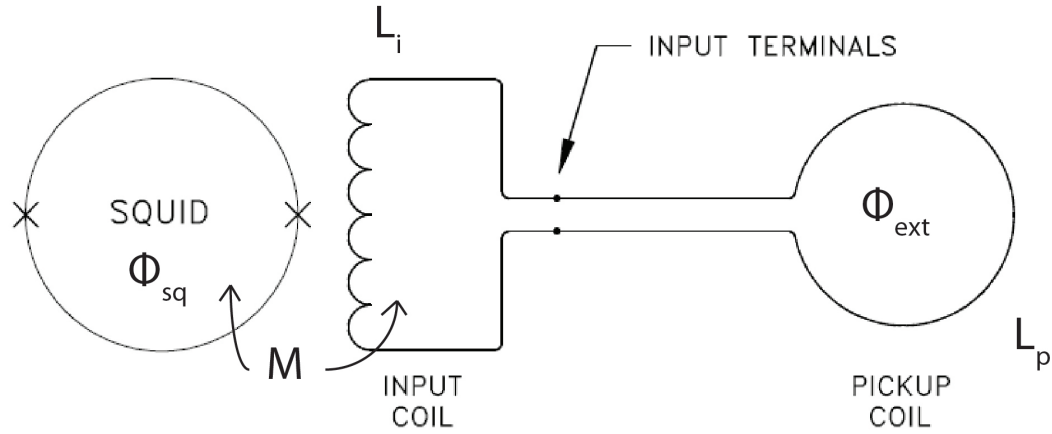


Figure 3.7: Quantum Design dc SQUID circuit



main characteristics of this type of sensor are

- Operating Temperature: $< 1 \text{ K} - 7 \text{ K}$
- Input Inductance: $1.9 \mu\text{H}$ Nominal
- Input Sensitivity: $0.2 \mu\text{A}/\Phi_o$
- Modulation Coil Inductance: $0.07 \mu\text{H}$ Nominal
- Modulation Coil Sensitivity: $1.5 \mu\text{A}/\Phi_o$
- Effective SQUID Bias Current: $15 - 30 \mu\text{A}$
- Modulation Frequency: 500kHz Nominal item Output Frequency Range: $200\text{kHz} - 1\text{MHz}$

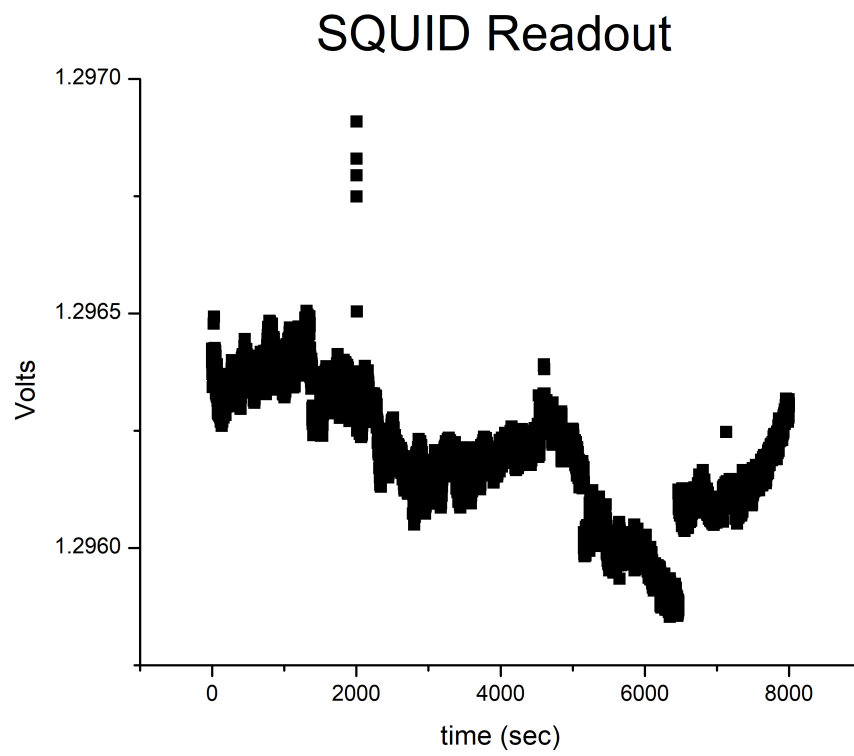
The flux through the SQUID and the flux through the pick up coils are connected through

$$\Phi_{ext} = (L_p + L_i) \frac{\Phi_{sq}}{M_i}, \quad M_i = k\sqrt{L_i L_{sq}}. \quad (3.1)$$

Optimizing this equation with respect to L_i reveals that the most efficient coupling happens when $L_i = L_p$. This acts as a guide to how the pick up coils should be constructed.

The pick up coils immediately surround the outer vacuum jacket and are two 2-4-2 second order gradiometers whose coils are separated by 1 cm. The gradiometers, comprised of AWG 24 NbTi wire, are set into a 1.1 cm diameter 20 cm long G10 cylinder which screws into a base attached to the chassis. This results in a pick up coil induction of $\sim 2 \mu\text{H}$. The center coils of the two gradiometers are separated by 6 cm. This was found to be sufficient separation to prevent inductive coupling between the coils which had plagued earlier configurations. Single core wire is used as opposed to multi-filament. The use of multi-filament wire for the gradiometers resulted in a SQUID readout beset with many jumps in value which masked the actual signal from the sample. We postulate that this was caused by multiple Josephson Junction decays created by poor connectivity between the filaments. The sample, whose vertical position can be adjusted during operation from the top of the sample holder protruding from the top of the chassis, is placed directly in the center of one of the gradiometers.

Figure 3.8: Bare SQUID signal, $1 \Phi_o/V$, on a 1 kHz filter with pickup coil terminals shunted



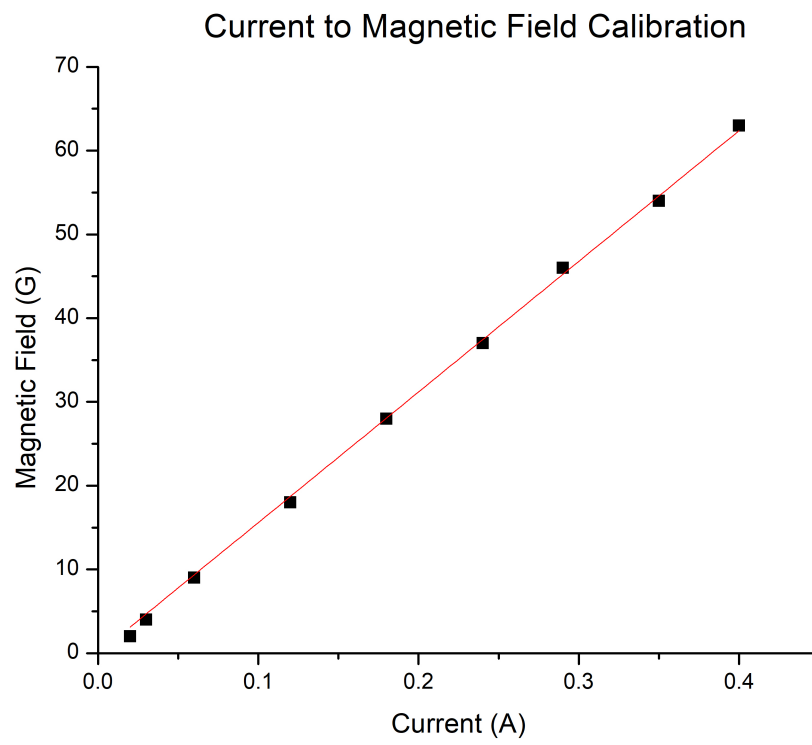
The two sets of gradiometer wires are fed into the compartment directly above the pickup coils into two SQUIDs electrically shielded from the environment by superconducting lead foil. In between the coils and the SQUIDs, the NbTi wires are fed through Cu foil wrapped in Manganin wire, which, in turn, is fed to a power supply outside the experiment. In order to eliminate built up magnetic flux in the NbTi wire, immediately after the field is turned off and before data collection starts, current is sent through the Manganin wire heating the Cu foil and forcing the NbTi wire into its normal metallic state.

Directly surrounding the pick up coils is the magnetic field coil. Set in a G10 cylinder 4 cm in diameter and 20 cm long, approximately 320 turn/cm of 36 AWG copper wire provides the magnetic field for the experiment. The current to magnetic field calibration is performed on the bench noting that the resistance of the copper wire will decrease substantially at liquid helium temperatures. Both the magnetic field and SQUID wire heater wires run through relays that cut off when not in use to prevent noise from the power supplies from contaminating the experiment.

3.2 Experimental Protocol and Results

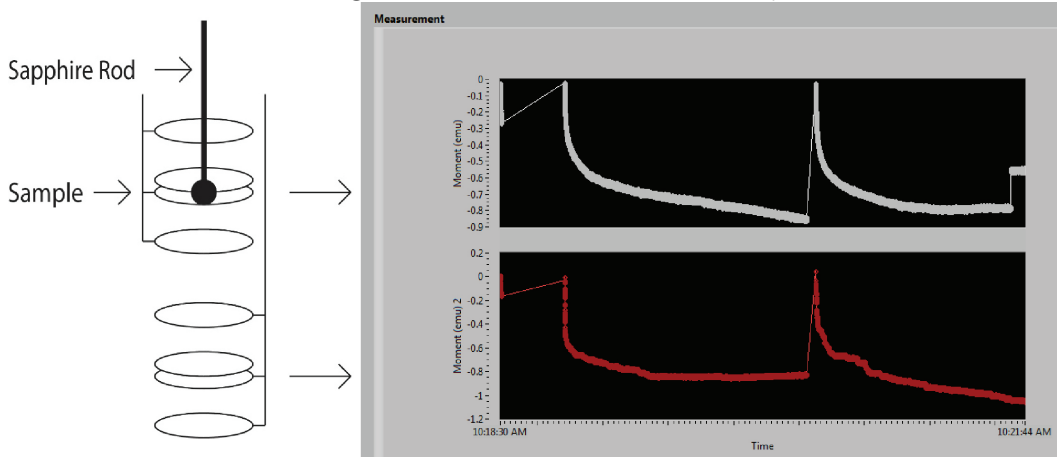
This magnetometer is built specifically to perform TRM measurements of spin glasses. As mentioned previously, it is the final points of the TRM decay that are most valid. But, through the use of both SQUIDs, it is possible to separate the environmental fluctuations from the sample signal. The correlation between drifts in the two SQUIDs was first noticed when a series

Figure 3.9: Current to Magnetic Field calibration performed with Gaussmeter resulting in 0.006 A/G



of particularly intense storms moved through the area.

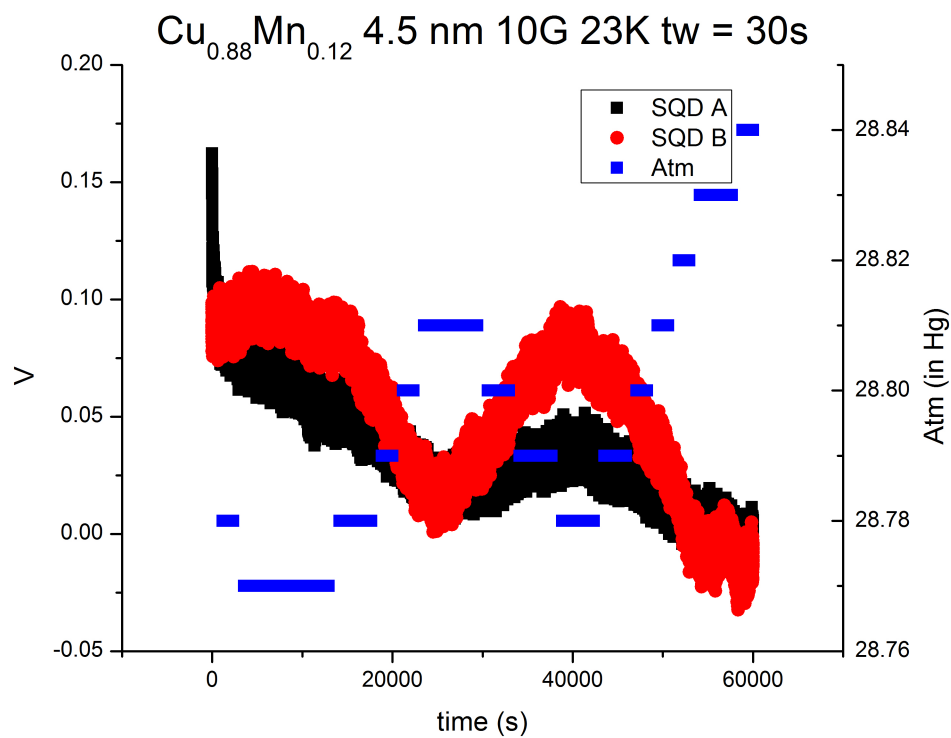
Figure 3.10: Simultaneous Readout from both SQUIDs one measuring the sample plus background fluctuations while the second only reads background fluctuations. Note the slight drifts found in the both SQUIDs.



These exaggerated fluctuations allowed for a calibrated subtraction of the environmental fluctuations from the sample signal. This belief was reinforced by, upon moving the sample into the second pick up coil, the reciprocal factor was successful in subtracting out the environmental fluctuations from the sample signal in the second SQUID.

Recent improvements on the chassis have allowed for pressure control in the liquid helium space and isolation from environmental factors. However, for most measurable temperatures in the 4.5 nm film less than T_f , the actual shape of the M_{TRM} loses its S(t) character. The remaining magnetization of the M_{TRM} after some standard measuring time is an equally well suitable measure of the waiting time effect in spin glasses and applicable when other measures are not. Since the final measures of the remaining M_{TRM} are valid regardless

Figure 3.11: CuMn 4.5 nm 10 G 23 K. This measurement provided our initial calibration for SQUID B subtraction from the sample signal in SQUID A.



of barometric fluctuations, they serve as the basis of the aging experiments in spin glass thin films presented in the following chapter.

Figure 3.12: CuMn 4.5 nm 20 G 18 K

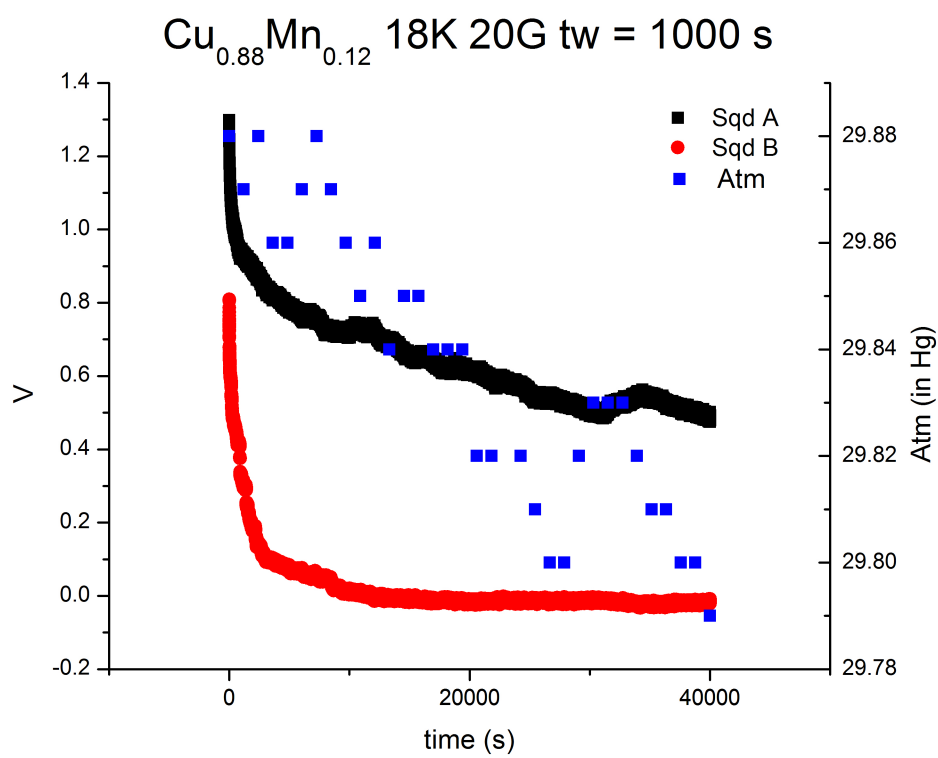


Figure 3.13: CuMn 4.5 nm 20 G 20 K

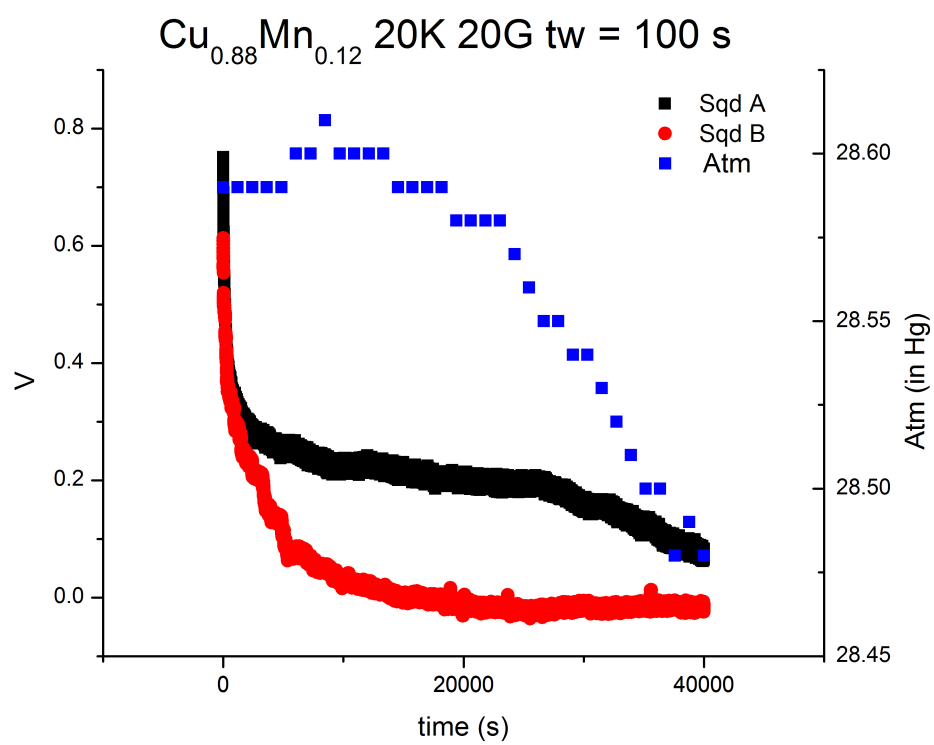
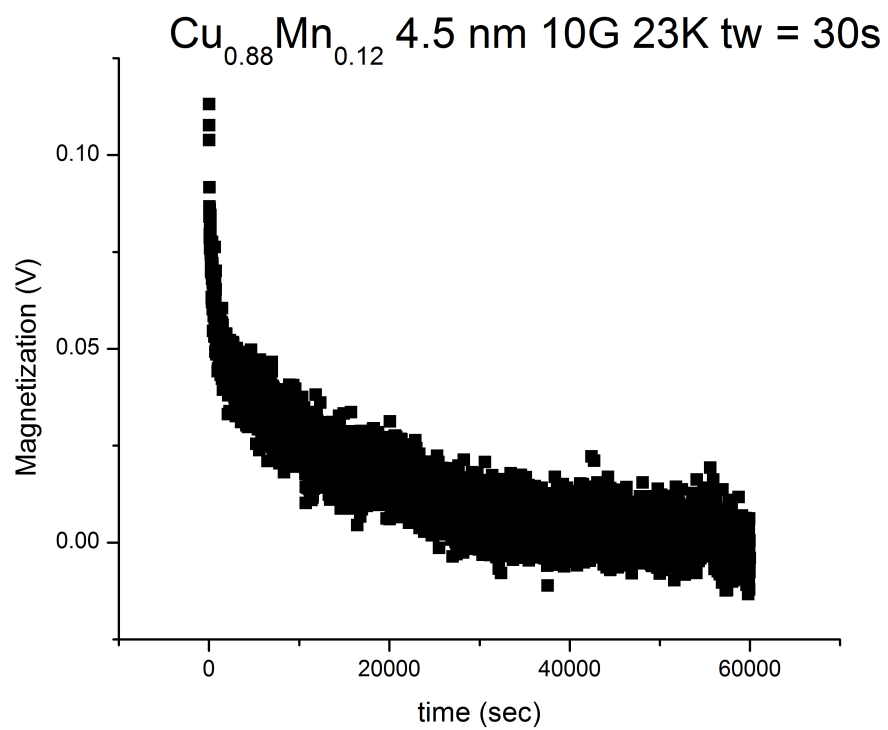


Figure 3.14: CuMn 4.5 nm 10 G 23 K corrected with SQUID B. Note that this is the same data set found in Figure 3.11.



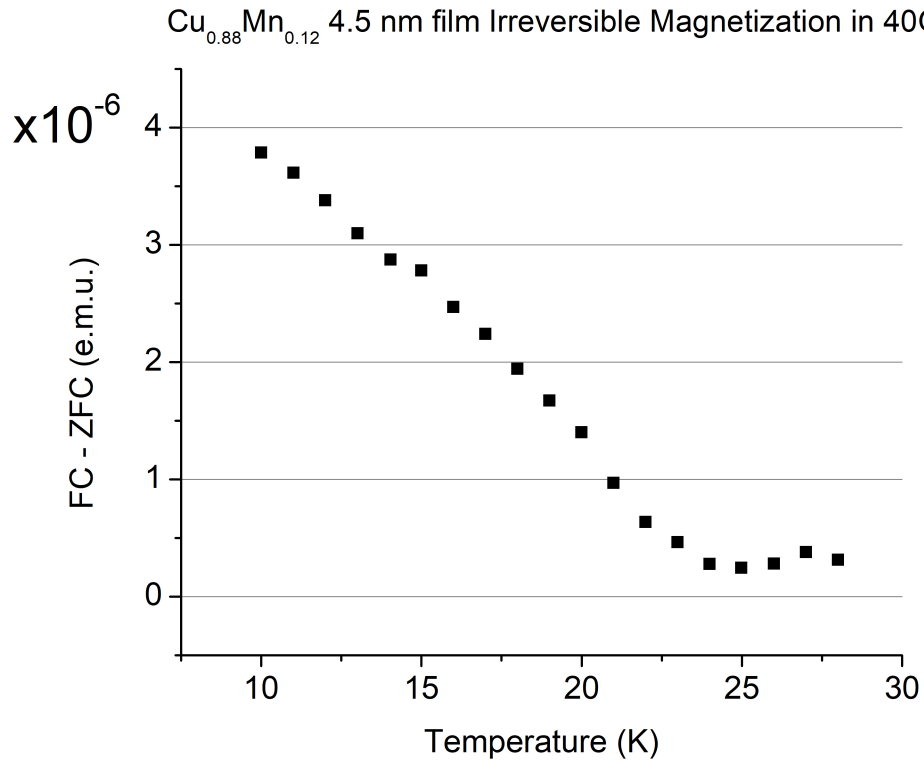
Chapter 4

Aging as Domain Growth

This chapter explicitly ties aging in the spin glass state to an associated length scale of correlated spins. In the thin film and bulk sample, the length scale is set by the film thickness and crystallite size respectively. The domain growth and associated waiting time effect saturate at a temperature and time scale predicted by power law dynamics [94]. The cessation of aging, as probed by the waiting time effect, provides a direct, model independent, measure of domain growth in the spin glass phase, as well as a demonstration of mesoscale dynamics in thin films. All TRM measurements in this chapter are taken at the home built SQUID magnetometer described in the previous chapter.

The effect of the waiting time is ‘imprinted’ on the spin glass state, and observed through the TRM decay. The decay for bulk samples is found to scale with t_w , up to temperatures $\sim 0.9T_g$, in a manner similar to polymers [16] such that the time-scaled decays fall onto one another [90]. Interpreted within the infinite dimensional mean field hierarchical model of Parisi [92], this time is representative of an exploration of configuration space across ever increasing energy barriers within the field cooled magnetization manifold. Upon cutting the applied magnetic field, the system finds itself out of equilibrium. The

Figure 4.1: $\text{Cu}_{0.88}\text{Mn}_{0.12}$, $T_f = 25$ K, Irreversible Magnetization in 40 G

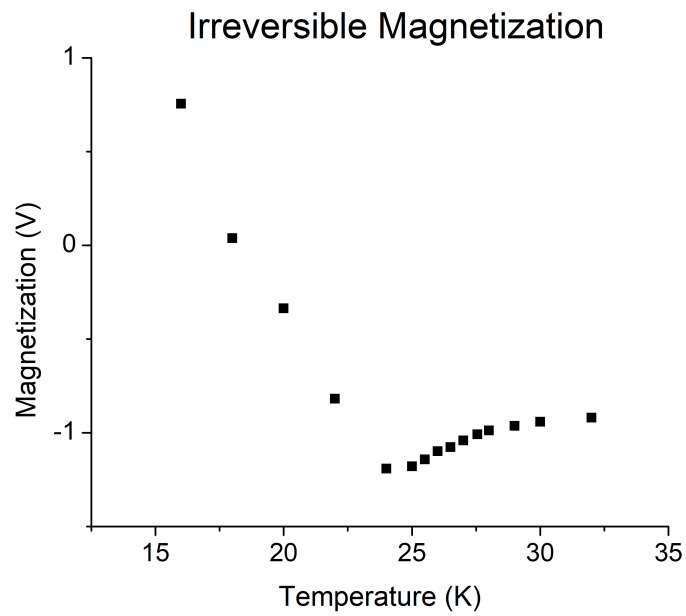


magnetization decay is dominated by the maximum energy barrier because of the high occupancy of states accessed during its initial state.

4.1 Experimental Techniques

The bulk $\text{Cu}_{0.97}\text{Mn}_{0.03}$ sample was made by alloying high purity Cu and Mn, then annealing at 900 C for 24 hours to randomize the Mn within the sample, followed by a rapid thermal quench to 77 K. The 4.5 nm $\text{Cu}_{0.88}\text{Mn}_{0.12}/\text{Cu}$ multilayer sample is the same as that used in the activation energy study.

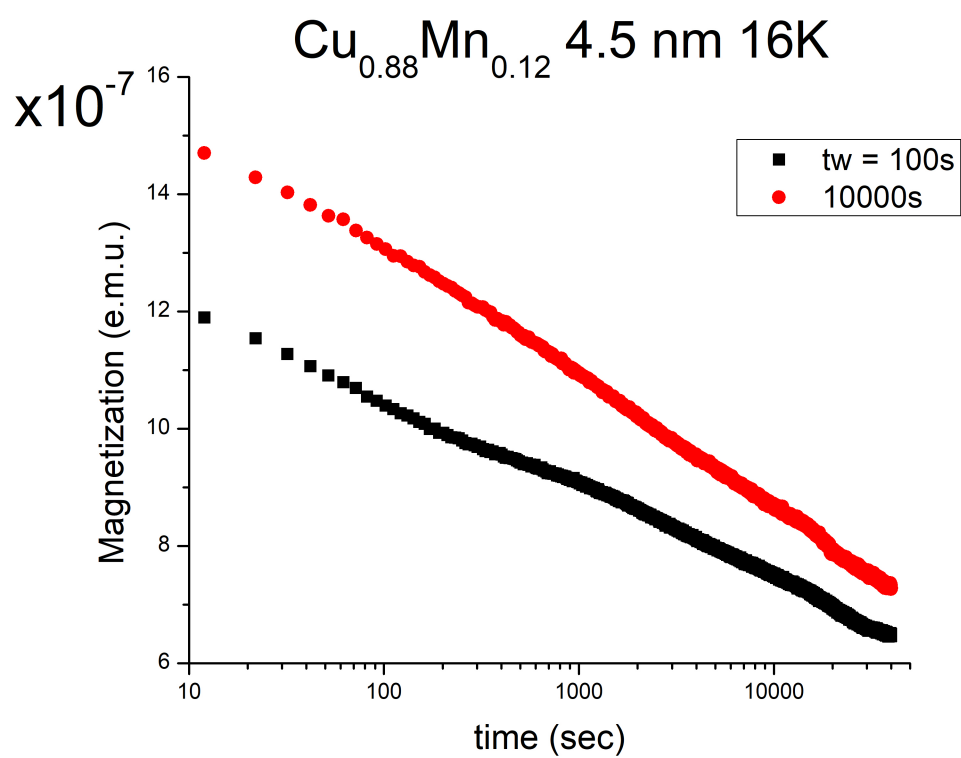
Figure 4.2: Bulk $\text{Cu}_{0.97}\text{Mn}_{0.03}$, $T_g = 25.6$ K, Irreversible Magnetization in 20 G. This measurement was taken as a series of short measurement times, 100s, TRMs at various temperatures and should only be used as a rough guide to what the irreversible magnetization should be.

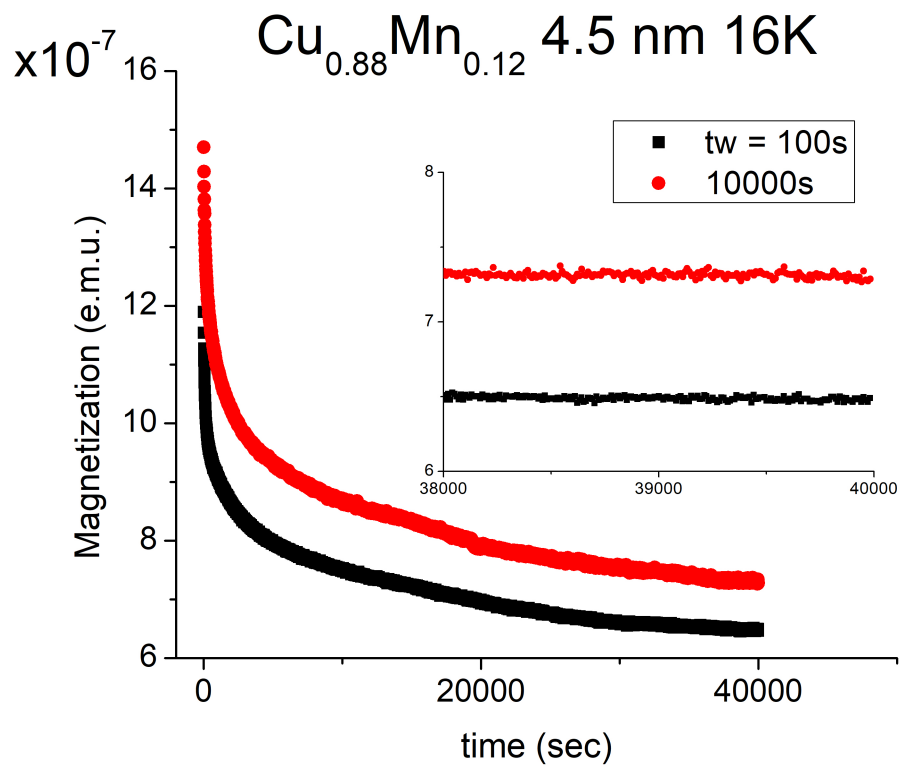


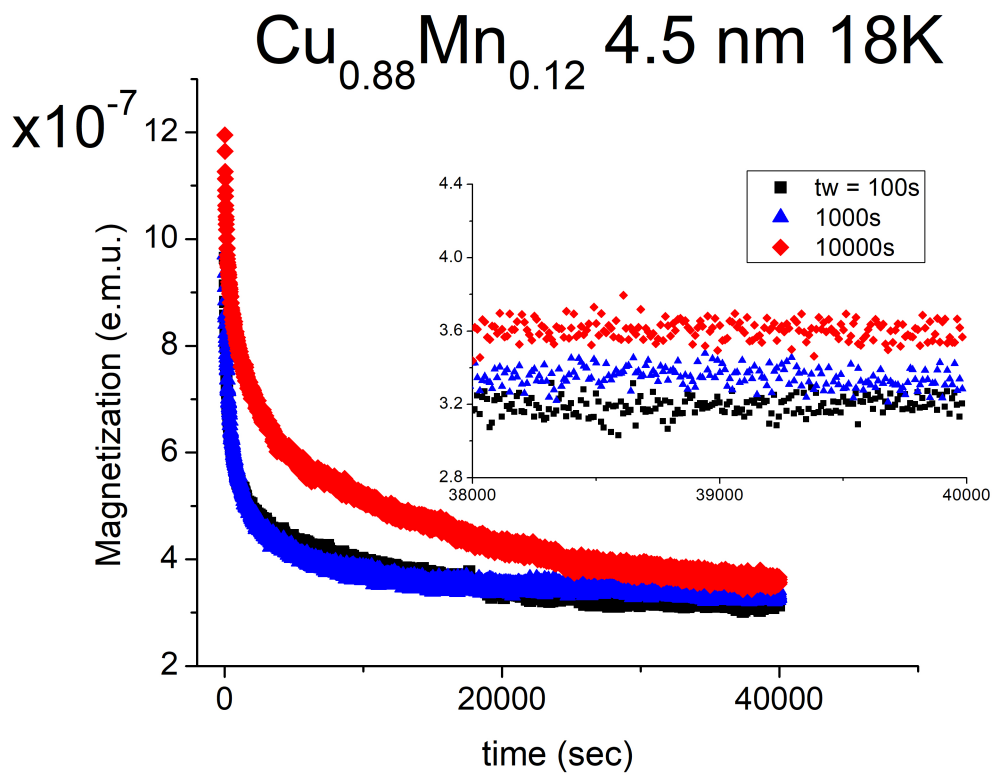
As mentioned in the previous chapter, fast cooling protocols were employed for the TRM measurements, reaching a stable T_m within 30-50 seconds of the temperature quench. The temperature at T_m was stable to a standard deviation of approximately 1 mK over the entire duration of the measurement, 20,000-40,000 seconds. TRM measurements were performed on both the bulk and multilayer samples over a wide range of temperatures and waiting times. The thin film spin glasses produced TRMs lacking in the obvious structure of their bulk counterparts [85]. Instead of using the inflection point of the decay as a measure of the effective waiting time, the remaining magnetization after a standard t_m is used as the measure of the aging effect.

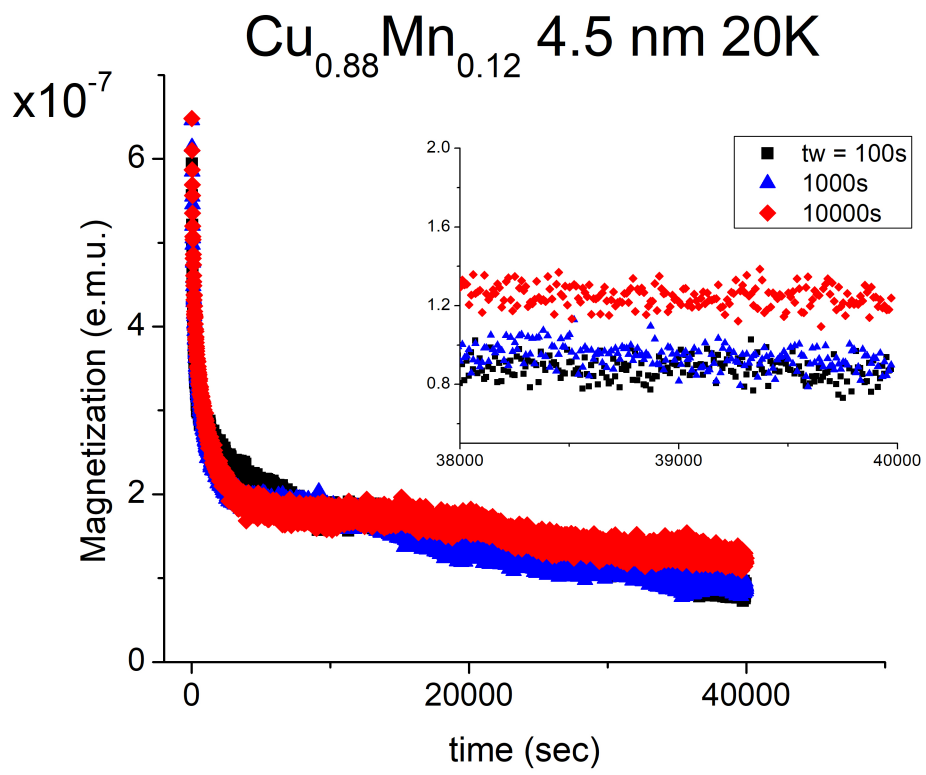
In addition to the lack of structure in the TRM decay for the films, there is another reason that the remaining remnant magnetization after t_m provides an appealing measure. Immediately following the TRM measurement, the temperature is raised above T_g and then re-cooled to T_m , all in the absence of the magnetic field, at which point the final magnetization is measured. This provides a ‘magnetic zero’ that includes the zero field paramagnetic magnetization along with any ambient background field. It is reasonable to assume that the background conditions haven’t changed appreciably in the few minutes between the last points of the TRM and sampling the magnetic zero [97]. This provides a reliable reference for the remnant magnetization at T_m .

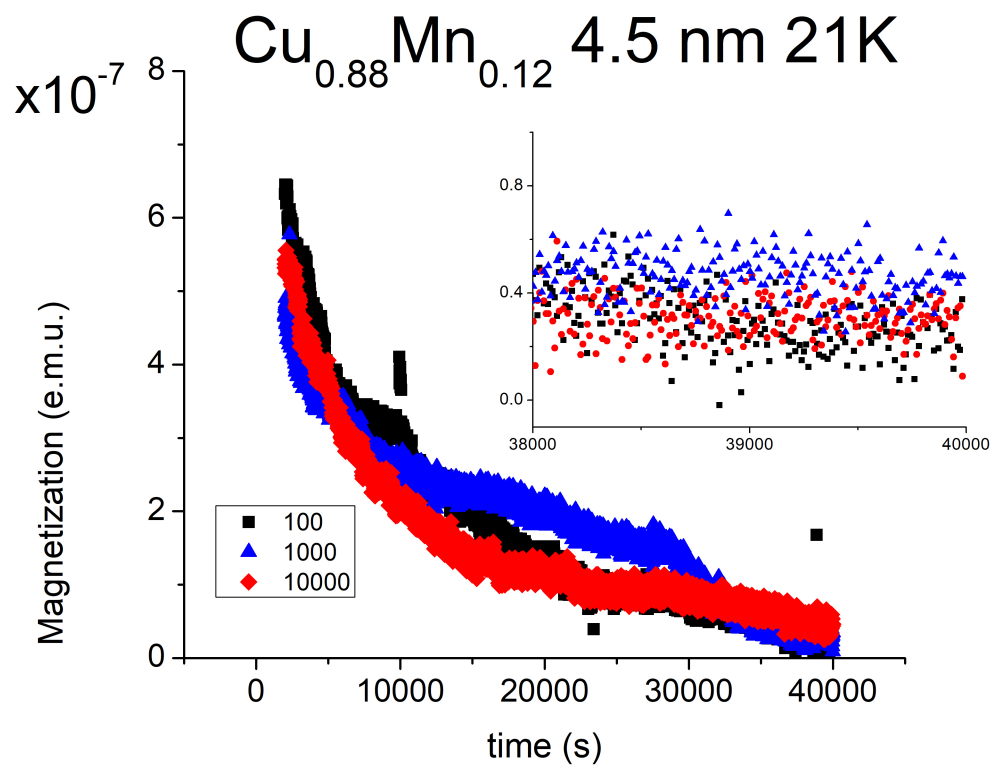
Figure 4.3: $\text{Cu}_{0.88}\text{Mn}_{0.12}$ TRM decays on a logarithmic scale



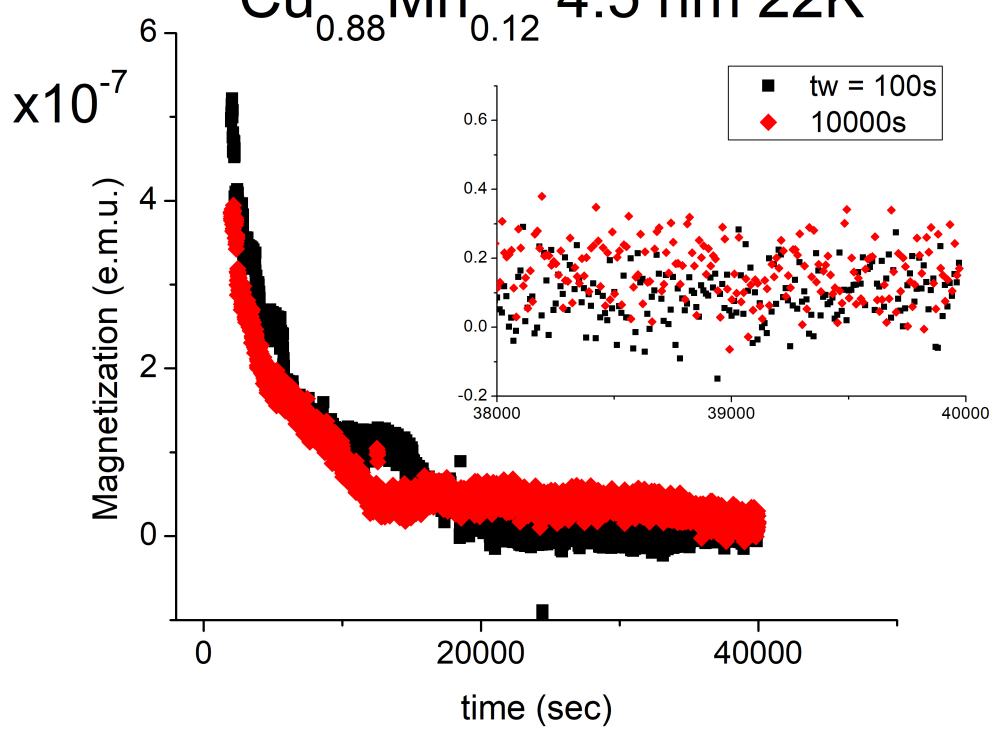








Cu_{0.88}Mn_{0.12} 4.5 nm 22K



4.2 Experimental Results

The TRM decays of the 4.5 nm multilayer film are displayed from 16 K to 22 K, the range of aging in the film. The final 2,000 seconds of the $\text{Cu}_{0.88}\text{Mn}_{0.12}$ film TRM are displayed in their insets for waiting times of 100, 1000, and 10000 sec.. The waiting time effect is readily seen in the separation of the remnant magnetization. For lower temperatures, 16 - 20 K, the waiting time has an obvious effect on the decays, whereas by 22 K, or $0.9T_f$, the waiting time has no effect on the decays.

The final point of the TRMs are displayed in Fig. 4.4. For the film, in Fig. 4.4b, the final points come together at 22 K and upward. At lower temperatures, the waiting time effect is shown by the separation of points. The time dependence of the T_f can be seen in the 23.5 K points where the TRM has decayed to zero. At this temperature, the relaxation time has been surpassed by the measuring time of 40,000 s.

For the bulk sample, the waiting time effect, as observed through the final magnetization of the TRM, persists up to $0.98T_g$. This large disparity in waiting time effect is but one time dependent difference between the bulk and the film. For temperatures below T_g in the bulk, the TRM is never seen to completely decay. This illustrates, as far as our measurement capabilities go, the true nature of the bulk transition in terms of a divergent activation energy.

In addition to considering the TRM magnetization after a standard

measuring time, the $S(t)$ curves of the bulk TRMs were also analyzed.

$$S(t) = -\frac{\partial M(t, t_w, T)}{\partial \ln t} \quad (4.1)$$

The $S(t)$ curves track the inflection point of the TRM as a function of waiting time and temperature on a logarithmic time scale. The $S(t)$ curve is seen as a more transparent microscope into the dynamics of the system as it represents the distribution of relaxation times present in that decay.

$$TRM(t, t_w, T) = \int_{\tau_o}^{\infty} m_o(t_w) g(\tau) e^{-t/\tau} d\tau \quad (4.2)$$

$$\begin{aligned} S(t)_{t_w, T} &= -\frac{\partial TRM(t, t_w, T)}{\partial \ln t} = m_o(t_w) \int_{\tau_o}^{\infty} g(\tau) \frac{t}{\tau} e^{-t/\tau} d\tau \\ &\simeq m_o(t_w) \int_{\tau_o}^{\infty} g(\tau) \delta(\tau - t) d\tau = m_o(t_w) g(t) \end{aligned} \quad (4.3)$$

The $S(t)$ curves track the effective waiting times of the bulk sample. For low temperatures, less than $0.77T_g$, the effective waiting times are approximately twice the actual waiting times. The effective waiting times very gradually decrease to just less than the actual waiting times until $0.9T_g$. At this temperature up to $0.95T_g$, the effective waiting times rapidly drop to a common value less than 100 s.

4.3 Discussion

These results suggest that aging in these spin glass samples is intimately tied to growth of domains which evolve in the form of power law dynamics. The

correlation length, ξ , represents the radius of a correlated spin glass domain which grows until it reaches either the film width in the multilayer samples or crystallite edge for the bulk sample, at which point the maximum energy barrier is reached.

The traditional way of producing metallic spin glasses such as CuMn and AgMn is to thoroughly alloy the sample, then anneal at high temperature to randomize the Mn within the sample followed by a rapid thermal quench to 77 K or 273 K to avoid phase separation. This however has the effect of producing samples with very small crystallites. Employing Debye-Scherrer analysis, x-ray diffraction measurements of the bulk sample find a mean crystallite size of 80 nm.

$$\tau = \frac{K\lambda}{\beta \cos \theta} \quad (4.4)$$

The width of the crystallite is represented by τ , K is the unitless factor 0.95, λ is the x-ray wavelength, the full width at half max is β and θ is the diffraction angle. These results were confirmed using SEM analysis of crystallites on the surface. Looking at 10 different crystallites, 8 of them were found to be within 10 nm of 80 nm. One smaller crystallite 60 nm and a much larger crystallite, 800 nm were also found. It is clear there exists a distribution of crystallite sizes in the sample but a large percentage are around 80 nm. This length will be used for further analysis.

By using the two different thicknesses, 80 nm for the bulk, and 4.5 nm for the thin film, and the relevant t_{co} , we can solve for c_1 and c_2 . For the bulk, we take the collapse of the waiting time to occur at $T = 25.4$ K, $t_{co} = 100$ s,

and $\mathcal{L} = 80$ nm. For the thin film, we take the collapse to occur at $T = 22$ K, $t_{co} = 100$ s, and $\mathcal{L} = 4.5$ nm. From Chapter 2, $1/\tau_0 = 6.9 \times 10^{12} \text{ s}^{-1}$ and $a_0 = 0.523$ nm for the Mn concentration of 11.7 at.%. The bulk sample used in this paper has a Mn concentration of 3 at.%, so scaling by concentration results in $1/\tau_0 = 3.35 \times 10^{12} \text{ s}^{-1}$ and $a_0 = 0.819$ nm. This results in $c_1 = 1.401$ and $c_2 = 0.128$. These values are close to previously calculated ones [30].

For the 4.5 nm film sample in particular, finite size effects become important. The fact that the surface area to volume ratio is appreciable causes us to consider the effect of correlation length nucleation points close to the surface of the film. For the bulk sample, the crystallite sizes are large enough to neglect edge effects. To calculate an effective crossover time as a function of temperature, assume a uniform distribution of nucleation sites across the film width.

$$\xi(t, T) = a_0 c_1 \left(\frac{t}{\tau_0}\right)^{c_2 \frac{T}{T_g}} \quad (4.5)$$

A simple average of crossover times results in an effective cross-over time,

$$t_{co}^{eff}(T) = \frac{2}{L} \int_{L/2}^L dx t_{co}(x, T), \quad (4.6)$$

where L is the film thickness.

Figure 4.14 illustrates an effective phase diagram. The boundary divides the system into a spin glass phase with aging and a glassy state that does not exhibit aging behavior. It is important to keep in mind that this is an effective phase diagram in the sense that the boundary is dependent on the length scale of the experiment. This prediction roughly agrees with the

suppression of the waiting time effect in these films. This analysis provides an experimental check on the growth of the correlation length as well as the spatial distribution of nucleation centers, which we assumed to be uniform in this case. Note that this analysis only applies in the range $L/2 < \xi < L = 4.5$ nm.

The growth of the correlation length has been found to be consistent with power law dynamics over a range of experiments. From the work of Kenning [87], it is shown that, while c_1 and c_2 are material dependent constants, they are independent of concentration. Combining the freezing temperatures from different Mn concentrations and film thicknesses shows a universal agreement, at least amongst CuMn/Cu multilayers, to

$$\frac{T_f}{T_g} c_2 \ln\left(\frac{t_{co}}{\tau_o}\right) + \ln c_1 = \ln\left(\frac{L}{a_o}\right). \quad (4.7)$$

Using realistic cool down and measurement times, similar to those described in Chapter 2, values of c_1 and c_2 are obtained and displayed below. That similar growth, through the value of c_2 , was found in different CuMn multilayers, fabricated decades apart from one another, provides some real validity to the idea of power growth dynamics.

Using the values of c_1 and c_2 derived from the aging experiments in Fig. 4.5, the growth of the correlation length is plotted as a function of waiting time, t_w , using the bulk T_g (53 K) as well as average distance between Mn atoms for 11.7% concentration. The dashed line corresponds to the thickness of the film. The absence of aging observed in the timescale $0.9 T_f$ to T_f indicates that

Table 4.1: Values for c_1 and c_2 over a range of experiments.

Experiment	c_1	c_2
T_f [87]	0.73 ± 0.06	0.114 ± 0.004
T_f [30]	0.58 ± 0.02	0.124 ± 0.002
Activation Energies [30]	1.5 ± 0.2	0.104 ± 0.003
Waiting time	1.40 ± 0.04	0.128 ± 0.004

during the waiting time, for each of the waiting times, the sample has reached the size limit imposed by the thickness of the thin film. The dynamics are therefore governed by a single large barrier which then defines an Arrhenius law for the decays. While the waiting time effect has ended we still observe glassy dynamics in the TRM decay.

Another measure of the growth of correlations is found in the $S(t)$ data. Again, finite size effects constrain the the growth of correlations as evidenced by the $S(t)$ curves, for different waiting times, collapsing onto one another as the glass temperature is approached. The particular shape of the curves found in Figure 4.11 could be used to extract more nuanced information about the distribution of crystallite sizes in the bulk sample.

For two different spin glass samples, one bulk and one thin film, both of separate concentrations, we have demonstrated that their aging is representative of domain growth. It is perhaps surprising that the power law form of correlated regions works as well as it does. Reiger [33] only probed temperature scales up to $0.7T_g$. One would think this form would be modified so close to the critical temperature. In addition, high temperature bulk TRM de-

cays, between $0.9T_g$ and T_g , are known to differ from their lower temperature counterparts. They lose their well defined waiting time characteristics. We can interpret this by noting that smaller crystallites will have fully saturated much earlier than the waiting time and instead are representative of a range of relaxation times associated with the distribution of crystallite sizes.

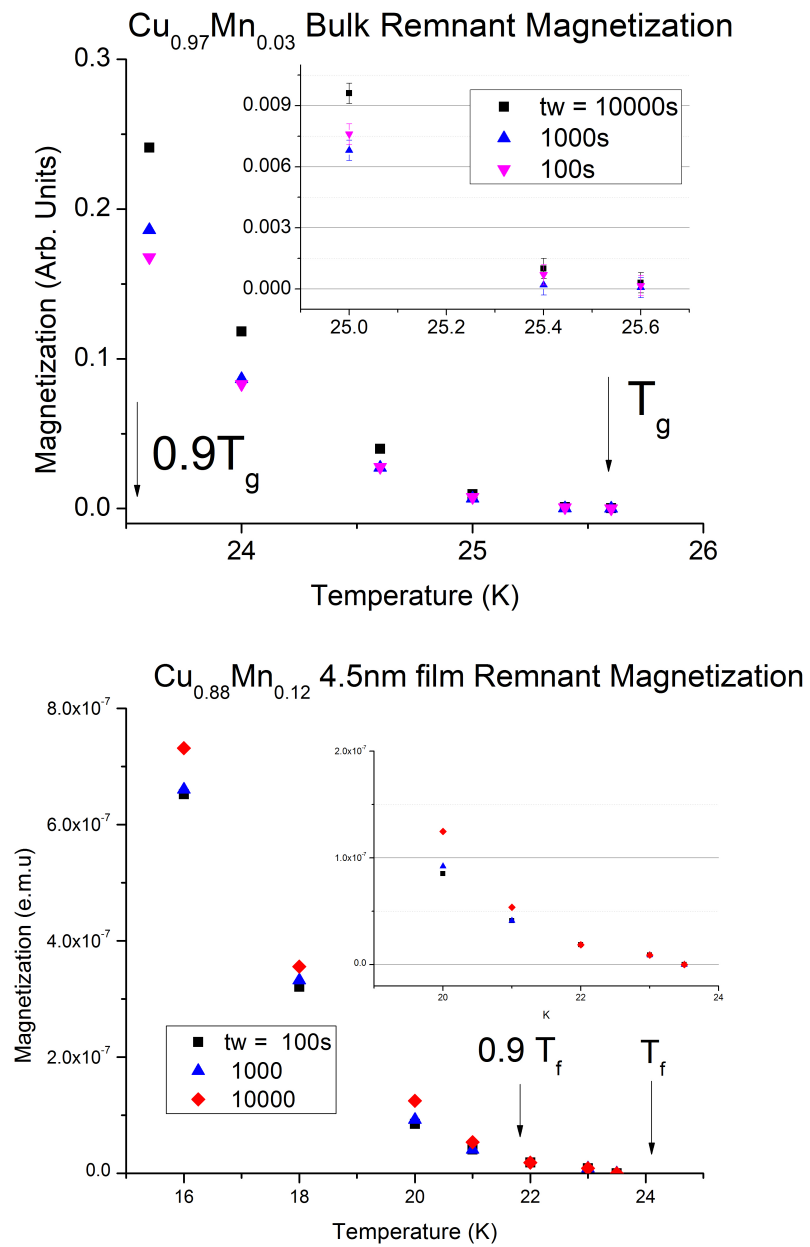


Figure 4.4: a) Remanence taken at 40,000 s for bulk $\text{Cu}_{0.97}\text{Mn}_{0.03}$. T_g for $\text{Cu}_{0.97}\text{Mn}_{0.03}$ is 25.6 K b) Remanence taken at 40,000 s for a multilayer $\text{Cu}_{0.88}\text{Mn}_{0.12}$ (4.5nm)/ Cu (60nm). Bulk T_g for the $\text{Cu}_{0.88}\text{Mn}_{0.12}$ is 54 K.

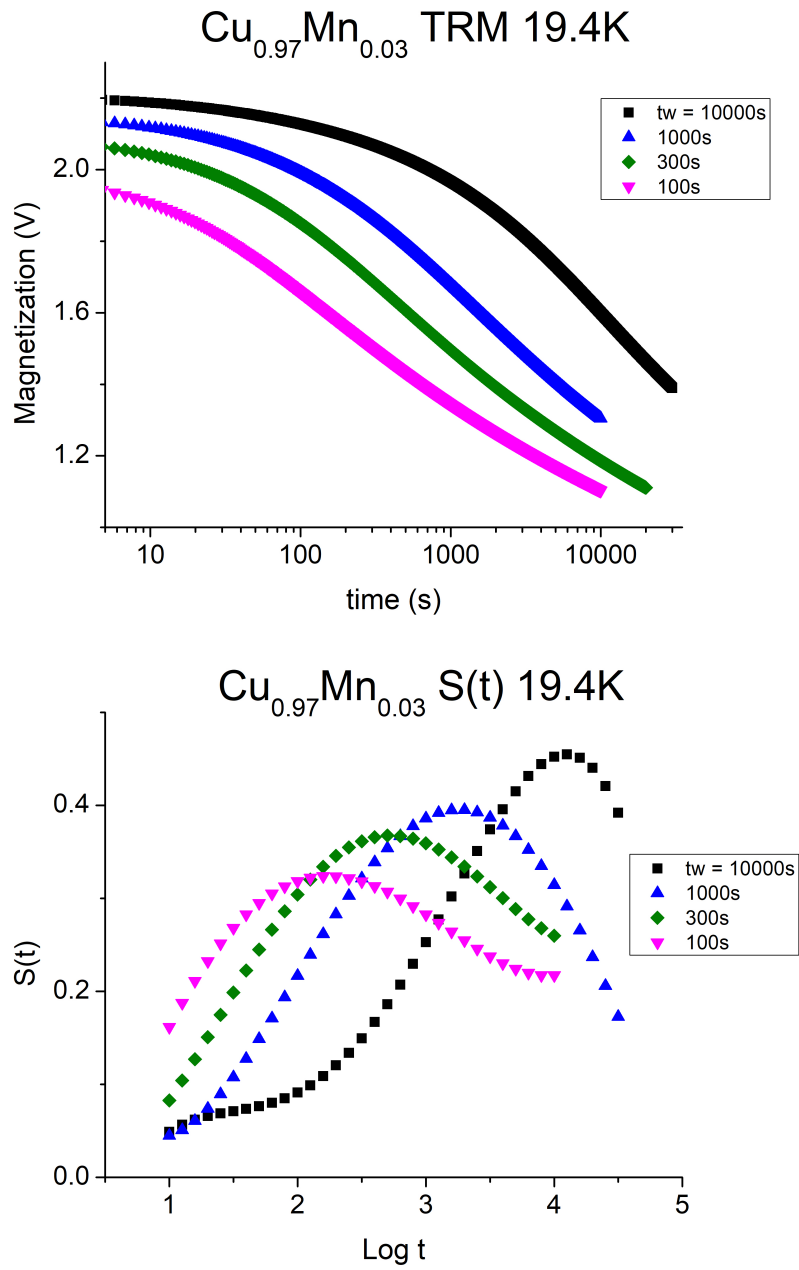


Figure 4.5: $\text{Cu}_{0.97}\text{Mn}_{0.03}$, $T_g = 25.6$ K, Waiting Time Experiments

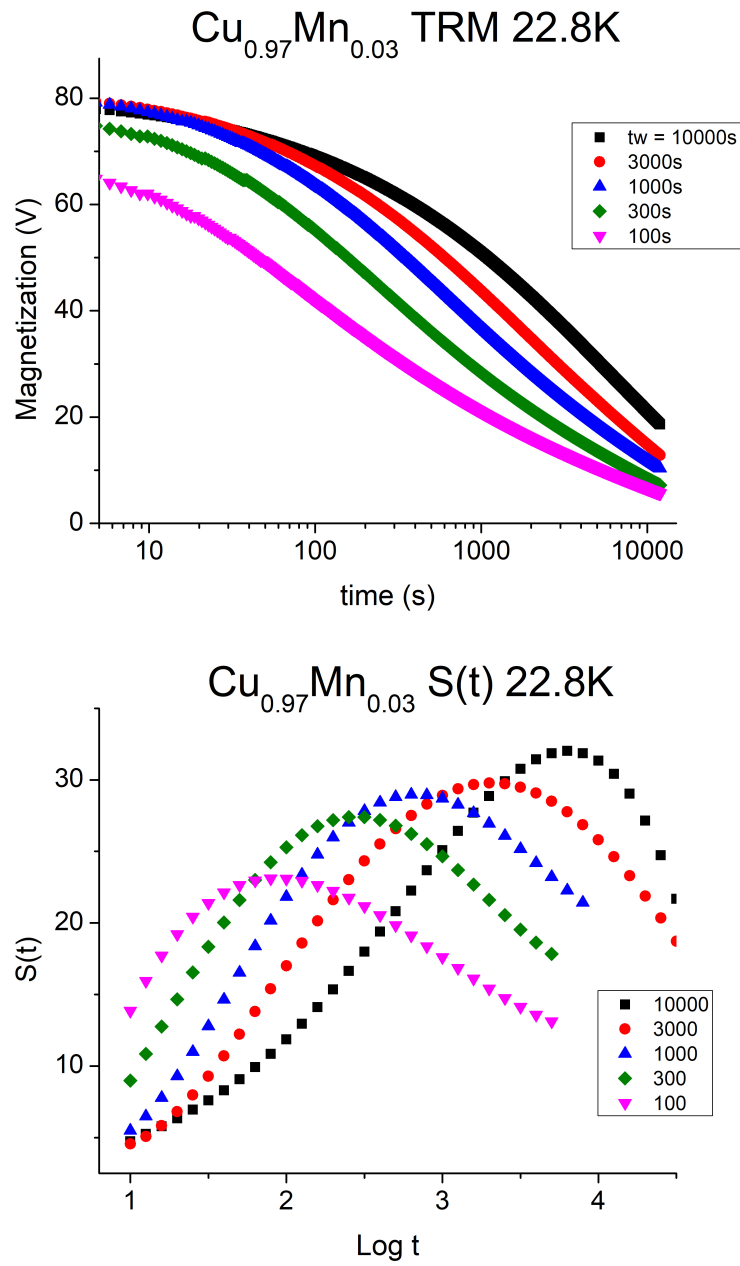


Figure 4.6: $\text{Cu}_{0.97}\text{Mn}_{0.03}$, $T_g = 25.6$ K, Waiting Time Experiments

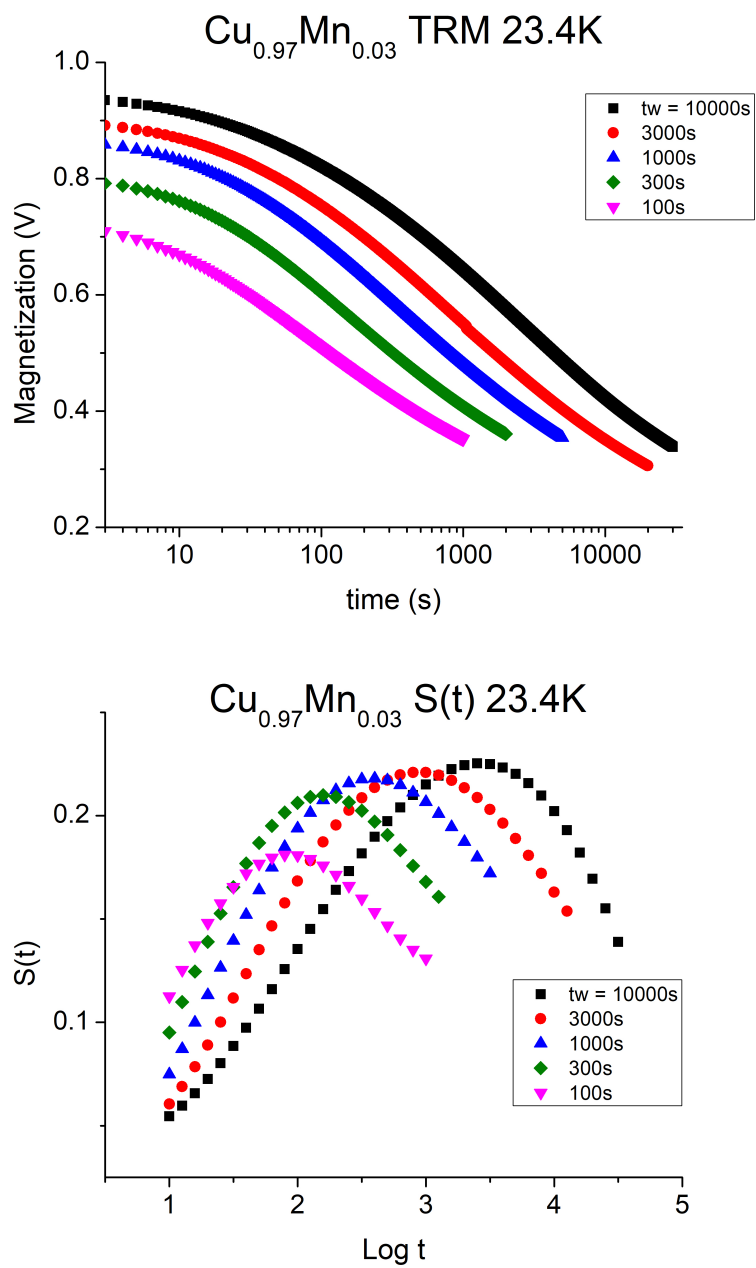


Figure 4.7: $\text{Cu}_{0.97}\text{Mn}_{0.03}$, $T_g = 25.6$ K, Waiting Time Experiments

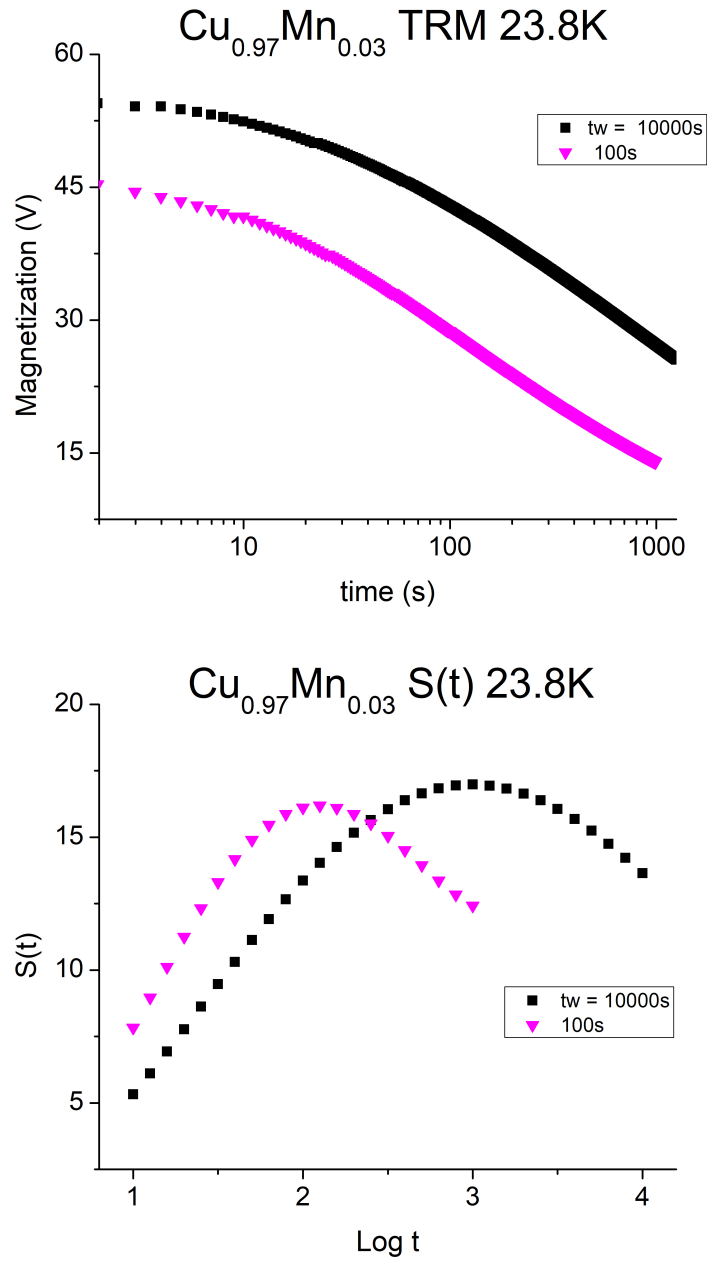


Figure 4.8: Cu_{0.97}Mn_{0.03}, $T_g = 25.6$ K, Waiting Time Experiments

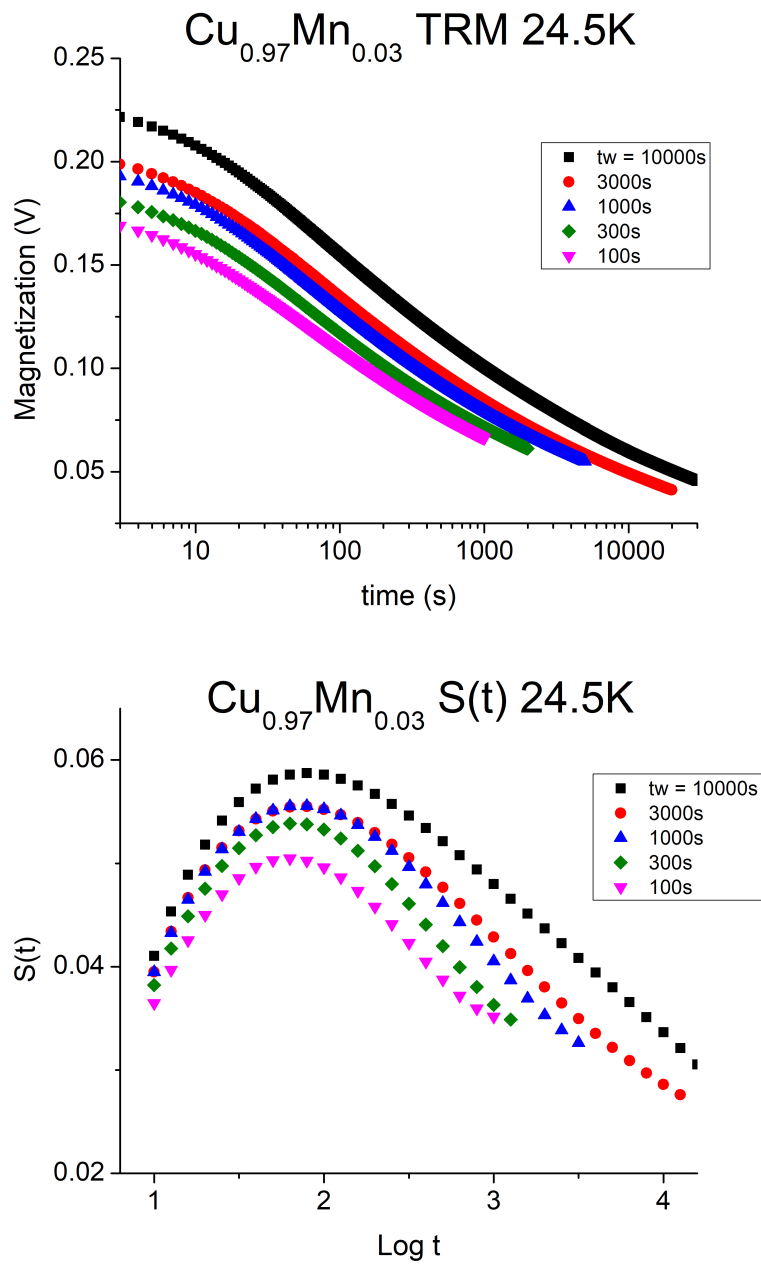


Figure 4.9: $\text{Cu}_{0.97}\text{Mn}_{0.03}$, $T_g = 25.6$ K, Waiting Time Experiments

Figure 4.10: $\text{Cu}_{0.97}\text{Mn}_{0.03}$, $T_g = 25.6$ K, Waiting Time Experiments

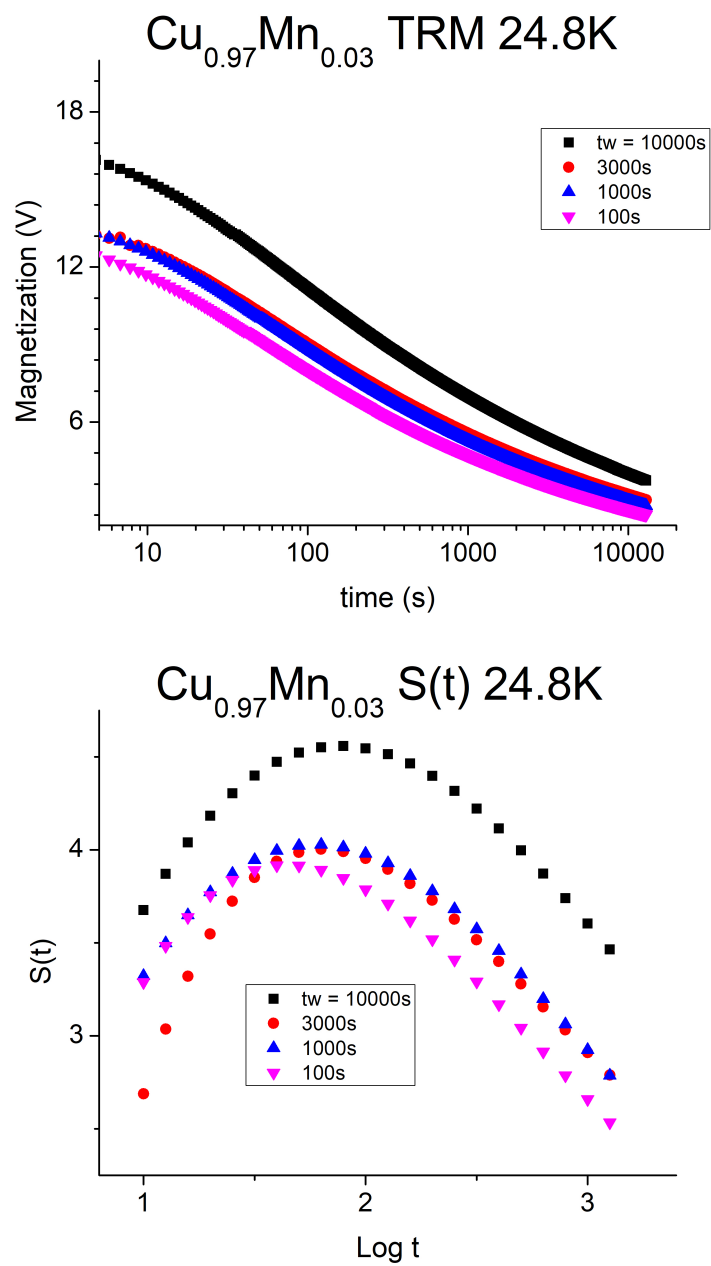
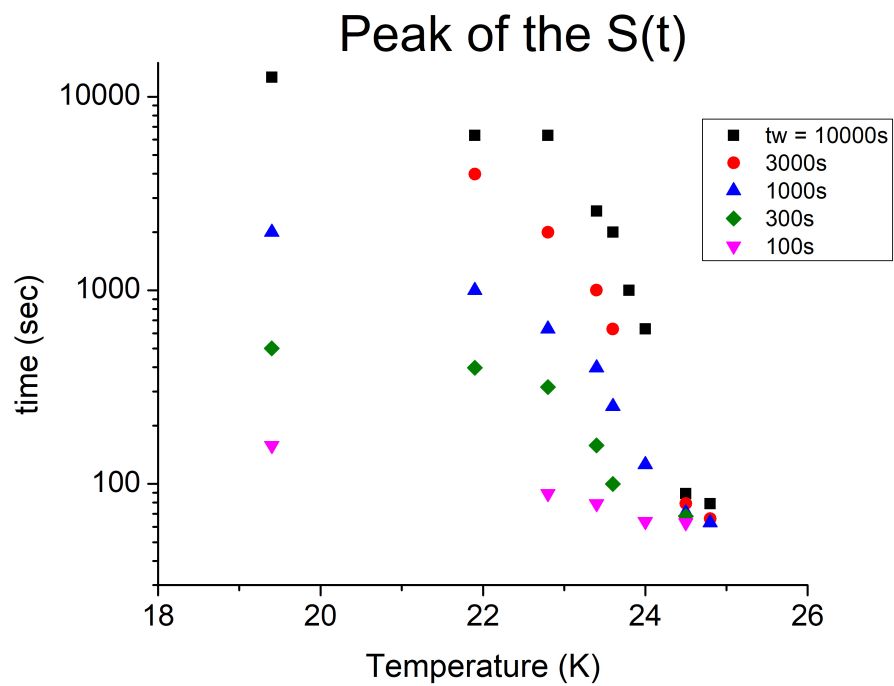


Figure 4.11: $\text{Cu}_{0.97}\text{Mn}_{0.03}$, $T_g = 25.6$ K collection of waiting time effects



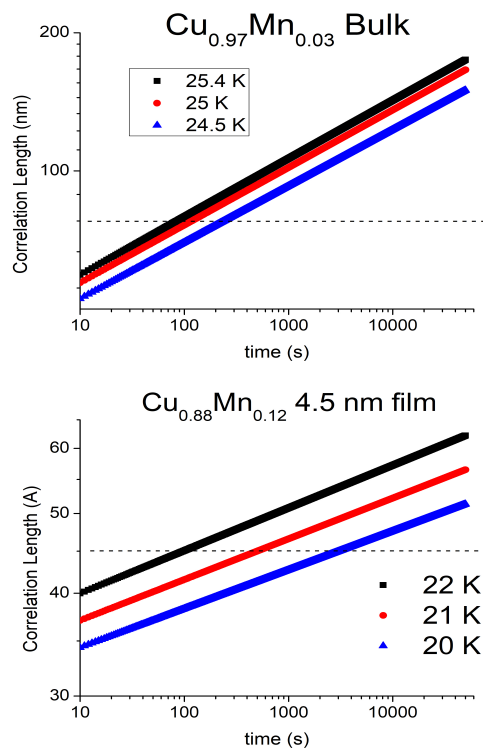


Figure 4.12: Fig. a) and b) show the power law nature of the correlation length growth. In Fig. a) and b), the dashed line represents the crystallite size and the film width respectively.

Figure 4.13: $f(\tau) = \frac{t}{\tau}e^{-t/\tau}$ for various values of t . For small t , the function is sharply peaked around t and will represent the distribution of relaxation times, $g(\tau)$, in the decay well. The curve at later times, being much more broadly peaked, will incorporate a large range of τ 's at a single point, $g(t)$, and not represent $g(\tau)$ as well. However, the peak of the $S(t)$ and the maximum of $g(\tau)$ remain valid measures of one another.

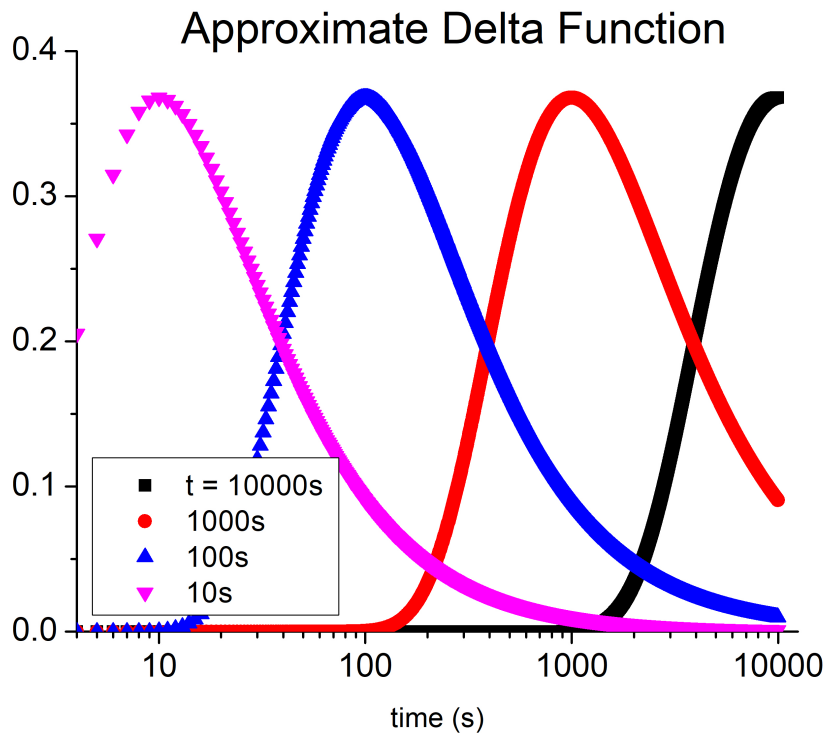


Figure 4.14: Effective Phase Diagram of CuMn 4.5 nm

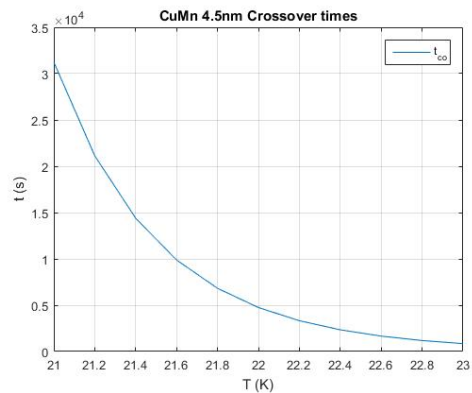
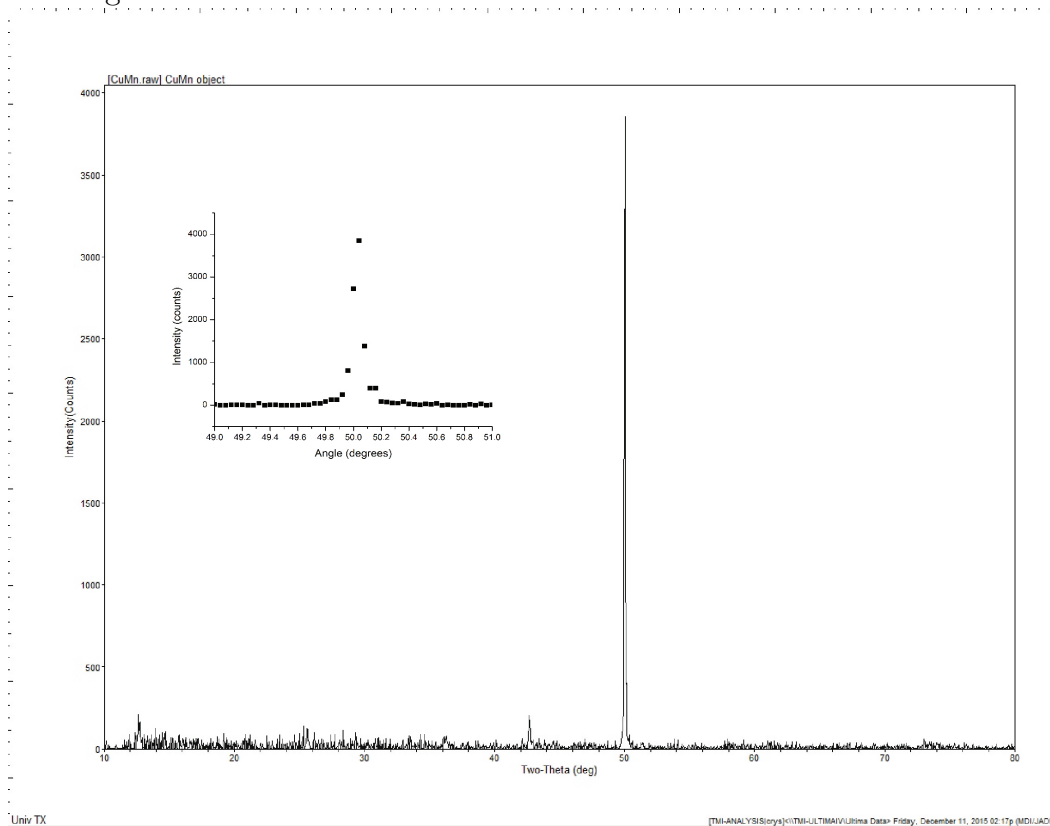


Figure 4.15: $\text{Cu}_{0.97}\text{Mn}_{0.03}$ X-ray Diffraction. The FWHM is approximately 0.15 degrees.



Chapter 5

Conclusion

This work has shown direct evidence that aging in spin glasses is a manifestation of the growth of correlated regions in this disordered material. Performing aging experiments in thin films of these materials provides a means of measuring domain structure where traditional methods such as neutron beam scattering yield null results.

To establish a connection between aging and the growth of correlated regions, some preliminary work was necessary. In Chapter 2, the nature of the growth of the correlated regions was established. Not only the form of the growth of correlations was established but the very nature of the ground state, or states. It was shown that the correlated regions grow in a manner consistent with a hierarchical model of an exponentially large number of ground states organized in an ultrametric geometry.

It is important to note the fundamental difference between this case and the one proposed by the droplet model. Were it found that correlations grew according to a power law, it would imply that there is one unique ground state. The range of activation energies, in this picture, would be due to various size excitations, regions of flipped spins, oscillating above this unique ground

state.

Due to our inability to fit the observed freezing temperatures or activation energies over a range of thin film widths to parameters in the context of the droplet model casts serious doubt on whether the spin glass phase of CuMn can be described in terms of that model. The use of three films widths actually over constrains the theory considerations. The crucial experimental prediction between the two models are how the maximum activation energies, or freezing temperatures scale with film width. The power law relationship, $\Delta_{max} \sim L^\psi$, following from the droplet picture, yields far too wide a spectrum of activation energies, or likewise, unrealistic time scales connected with the observed freezing temperatures. The logarithmic relationship, $\Delta_{max} \sim \ln(L)$, following from the hierarchical model, provides a natural explanation for the observed activation energies and freezing temperatures.

The second part of our investigation involved measuring aging through the waiting time effect for both a thin film sample as well as a bulk sample. Measuring the effects of aging in these multilayer thin films is not trivial. For one, the $S(t)$ character of the TRM decays is effectively masked by large edge effects. Other means of characterizing aging in these film, as well as bulk materials close to the glass temperature, needed to be developed. The use of the remaining magnetization after a standard measuring time was employed in Chapter 4. To precisely monitor that value, it was found that commercial SQUID magnetometry was inadequate. An in-house designed SQUID magnetometer, described in Chapter 3, was built to provide the resolution necessary

for the task at hand.

Quite different results for the waiting time effect experiments were found between the thin film and bulk samples. For the bulk, the waiting time effect persists up to $0.98 T_g$. For a true bulk, in the infinite size sense, one would expect the waiting time effect to exist up to the transition temperature. Indeed, the fact that it doesn't can be viewed as proof that the sample is comprised of finite size crystallites making up the bulk.

The 4.5 nm thin film displayed a different temperature dependence of the waiting time effect which ceases at $0.9 T_f$. Both the results of the film and the bulk can be interpreted as a correlation length reaching either the crystallite surface or film thickness. As such, waiting time experiments can be used as an accurate measure of the time and temperature dependence of the correlation length. The fact that it is possible to describe the observed correlation length growth with the power law dynamics predicted by the hierarchical model with very similar values of the exponential growth parameter, c_2 , provides further validation of this model. Repeating these experiments with various film widths will hopefully provide further validation of the ideas put forth in this work.

Bibliography

- [1] J. Owen, M. Browne, W. D. Knight, and C. Kittel, Phys. Rev. 102, 1501 (1956).
- [2] J. A. Mydosh, J. Magn. Magn. Mater. 7, 237 (1978).
- [3] V. Cannella and J. A. Mydosh, Phys. Rev. B 6, 4220 (1972).
- [4] For example, compared to the earlier work of O. S. Lutes and J. L. Schmit, Phys. Rev. 134, A676 (1964).
- [5] D. C. Vier and S. Schultz, Phys. Rev. Lett. 54, 150 (1985).
- [6] M. A. Ruderman and C. Kittel, Phys. Rev. 96, 99 (1954).
- [7] T. Kasuya, Prog. Theor. Phys. 34, 681 (1962).
- [8] K. Yosida, Phys. Rev. 106, 893 (1957).
- [9] J. Villain, Z. Physik B 33, 31 (1978).
- [10] G. E. Brodale, R. A. Fisher, W. E. Fogle, N. E. Phillips, and J. van Curen, J. Magn. Magn. Mater. 31-34, 1331 (1983).
- [11] D. C. Mattis, Phys. Lett. 56A, 421 (1976).
- [12] J. Chalupa, Sol. St. Comm. 22, 315 (1977).

- [13] L. P. Lévy and A. T. Ogielski, Phys. Rev. Lett. 57, 3288 (1986).
- [14] L. P. Lévy, Phys. Rev. B 38, 4963 (1988).
- [15] L. Lundgren, P. Svedlindh, P. Nordblad, and O. Beckman, Phys. Rev. Lett. 51, 911 (1983).
- [16] L.C.E. Struik, Physical aging in amorphous polymers and other materials, (Elsevier, Houston, 1978).
- [17] R. V. Chamberlin, Phys. Rev. B 30, 5393 (1984).
- [18] Non-ergodic in the sense that spatial averages across the sample at a single time do not equal temporal averages across infinite time at a single site. Include stat textbook.
- [19] S. F. Edwards and P. W. Anderson, J. Phys. F: Metal Phys. 5, 965 May (1975).
- [20] D. Sherrington and S. Kirkpatrick, Phys. Rev. Lett. 35, 26, 1793 (1975).
- [21] G. Parisi, J. Phys. A13, L115 (1980).
- [22] G. Parisi, J. Phys. A13, 1101 (1980).
- [23] G. Parisi, Phys. Rev. Lett. 50, 1946 (1983).
- [24] M. Mézard, G. Parisi, N. Sourlas, G. Toulouse, and M. Virasoro, J. Physique 45, 843 (1984).

- [25] M. Mézard and M. Virasoro, *J. Physique* 46, 1293 (1985).
- [26] D. S. Fisher and D. A. Huse, *Phys. Rev. Lett.* 56, 1601 (1986).
- [27] D. S. Fisher and D. A. Huse, *Phys. Rev. B* 38, 373 (1988).
- [28] D. S. Fisher and D. A. Huse, *Phys. Rev. B* 38, 386 (1988).
- [29] F. Lefloch, J. Hamman, M. Ocio, and E. Vincent, *EuroPhys. Lett.* 18, 647 (1992).
- [30] Q. Zhai, D. C. Henderson, D. Tennant, E. D. Dalhberg, G. G. Kenning, and R. L. Orbach, *Phys. Rev. B* 95, 054304 (2017).
- [31] N. E. Israeloff and M. B. Weissman, *Phys. Rev. Lett.* 63, 794 (1989).
- [32] K. A. Meyer and M. B. Weissman, *Phys. Rev. B* 51, 8221 (1995).
- [33] H. Rieger, *J. Phys. A: Math. Gen.* 26, L615 (1993); H. Rieger, B. Steckemetz, and M. Schreckenberg, *Europhys. Lett.* 27, 485 (1994).
- [34] A. J. Bray and M. A. Moore, *J. Phys. C: Sol. Stat. Phys.* 17, L463 (1984).
- [35] A. T. Ogielski and I. Morgenstern, *Phys. Rev. Lett.* 54, 928 (1985).
- [36] A. K. Hartmann and A. P. Young, *Phys. Rev. B* 64, 180404(R) (2001).
- [37] H. G. Ballesteros, A. Cruz, L. A. Fernández, V. Martín-Mayor, J. Pech, J. J. Ruiz-Lorenzo, A. Tarancón, P. Téllez, C. L. Ullod, and C. Ungil, *Phys. Rev. B* 62, 237 (2000).

- [38] S. Boettcher, Phys. Rev. Lett. 95, 197205 (2005).
- [39] S. Franz, G. Parisi and M.A. Virasoro, J. Phys. I (France), 4, 1657 (1994).
- [40] W. L. McMillan, J. Phys. C 17, 3179 (1984).
- [41] L. Lundgren, P. Svedlindh, and O. Beckman, Phys. Rev. B 26, 3990 (1982).
- [42] M. Alba, M. Ocio, and J. Hammann, Europhys. Lett. 2, 45 (1986).
- [43] V. Dupuis, F. Bert, J.P. Bouchaud, J. Hammann, F. Ladieu, D. Parker and E. Vincent, Pramana J. of Phys. 64, 1109 (2005).
- [44] G. F. Rodriguez, G.G. Kenning, R. Orbach, Phys. Rev. Lett. 91, 037203 (2003).
- [45] D. S. Fisher and D. A. Huse, Phys. Rev. Lett. 56, 1601 (1986).
- [46] G. C. Kenning, J. M. Slaughter, and J. A. Cohen, Phys. Rev. Lett. 59, 2596 (1987).
- [47] G. G. Kenning, J. Bass, W. P. Pratt, Jr., D. Leslie-Pelecky, L. Hoines, W. Leach, M. L. Wilson, R. Stubi, and J. A. Cowen, Phys. Rev. B, 42, 2393 (1990).
- [48] Concurrently, similar behavior was found in ac susceptibility measurements on the magnetically doped semiconductor CdMnTeCdTe. D. D. Awschalom, J. M. Hong, L. L. Chang, and G. Grinstein, Phys. Rev. Lett. 59, 1733 (1987).

- [49] R. Stubi, D. L. Leslie-Pelecky, and J. A. Cowen, *J. Appl. Phys.* 67, 5970 (1990).
- [50] C. Dekker, A. F. M. Arts, H. W. de Wijn, A. J. van Duynveldt, and J. A. Mydosh, *Phys. Rev. Lett.* 61, 1780 (1988).
- [51] A. G. Schins, A. F. M. Arts, and H. W. de Wijn, *Phys. Rev. Lett.* 70, 2340 (1993).
- [52] L. Sandlund, P. Granberg, L. Lundgren, P. Nordblad, P. Svedlindh, J. A. Cowen, and G. G. Kenning, *Phys. Rev. B* 40, 869 (1989).
- [53] S. Guchhait, G. G. Kenning, R. L. Orbach, and G. F. Rodriguez, *Phys. Rev. B* 91, 014434 (2015).
- [54] Y. G. Joh, R. Orbach, G. G. Wood, J. Hammann, and E. Vincent, *Phys. Rev. Lett.* 82, 438 (1999).
- [55] S. Guchhait and R. Orbach, *Phys. Rev. Lett.* 112, 126401 (2014).
- [56] S. Sahoo, O. Petravic, C. Binek, W. Kleemann, J. B. Sousa, S. Cardoso, and P. P. Freitas, *J. Phys. Cond. Matt.* 14, 6729 (2002).
- [57] S. Sahoo, O. Petravic, W. Kleemann, P. Nordblad, S. Cardoso, and P. P. Freitas, *Phys. Rev. B* 67, 214422 (2003).
- [58] H. G. Katzgraber, L. W. Lee, and A. P. Young, *Phys. Rev. B* 70, 014417 (2004).

- [59] Y. G. Joh, “Spin Glass Dynamics, Developing a Hierarchical Model from Experiment”, Thesis University of California, Riverside, 1997.
- [60] G. G. Wood, “Measurements of the Spin Glass Correlation Length and its Consequence from Finite Size Systems”, Thesis University of California, Riverside, 2000.
- [61] C. M. Rost, “Development of the Dual DC SQUID Magnetometer and Aging in Non-Equilibrium Dynamics”, Thesis Indiana University of Pennsylvania 2012.
- [62] Quantum Design, Inc.
- [63] Magnicon GmbH, Inc.
- [64] A. T. Rowley and A. Myers, *J. Phys. E: Sci. Instrum.* 20, 146 (1987).
- [65] K. G. Vandervoort, G. Griffith, H. Claus, and G. W. Crabtree, *Rev. Sci. Instrum.* 62, 2271 (1991).
- [66] T. J. Jackson, M. N. Keene, and C. E. Gough, *Meas. Sci. Technol.* 3, 988 (1992).
- [67] J. Magnusson, C. Djurberg, P. Granberg, and P. Nordblad, *Rev. Sci. Instrum.* 68, 3761 (1997).
- [68] D. Hérisson and M. Ocio, *Phys. Rev. Lett.* 88, 257202 (2002).
- [69] J. Clarke and A. I. Braginski, *The SQUID Handbook*, (Wiley, Weinheim, 2004), Sec. 5.6.

- [70] G. G. Kenning, D. M. Tennant, E. Rost, F. G. da Silva, B. J. Walters, G. Carenzo, Q. Zhai, D. C. Harrison, E. D. Dalhberg, and R. L. Orbach, Phys. Rev. Lett.
- [71] Y. G. Joh, “Spin Glass Dynamics, Developing a Hierarchical Model from Experiment”, Thesis University of California, Riverside, 1997.
- [72] G. G. Wood, “Measurements of the Spin Glass Correlation Length and its Consequence from Finite Size Systems”, Thesis University of California, Riverside, 2000.
- [73] C. M. Rost, “Development of the Dual DC SQUID Magnetometer and Aging in Non-Equilibrium Dynamics”, Thesis Indiana University of Pennsylvania 2012.
- [74] Q. Zhai, D. C. Harrison, and R. L. Orbach, Phys. Rev. B 96, 054408 (2017).
- [75] U. Larsen, Phys. Phys. Rev. B 33, 4803 (1986).
- [76] V. Cannella and J. A. Mydosh, Phys. Rev. B 6, 4220 (1972).
- [77] S. F. Edwards and P. W. Anderson, J. Phys. F 5, 965 (1975).
- [78] K. Binder and A. P. Young, Rev. Mod. Phys. 58, 801 (1986) and references therein.
- [79] L. Lundgren, P. Svedlindh, P. Nordblad, and O. Beckman, Phys. Rev. Lett. 51, 911 (1983); R. V. Chamberlin, Phys. Rev. B 30, 5393 (1984).

- [80] K. Jonason, E. Vincent, J. Hammann, J. P. Bouchaud, and P. Nordblad, Phys. Rev. Lett. 81, 3243 (1998).
- [81] M. Lederman, R. Orbach, J. M. Hammann, M. Ocio, and E. Vincent, Phys. Rev. B 44, 7403 (1991).
- [82] S. A. Werner, Sol. St. Comm. 56, 457 (1985).
- [83] A. K. Hartmann and A. P. Young, Phys. Rev. B 64, 180404(R) (2001).
- [84] C. Dekker, A. F. M. Arts, H. W. de Wijn, A. J. van Duynveldt and J. A. Mydosh, Phys. Rev. Lett. 61, 1780 (1988).
- [85] L. Sandlund, P. Granberg, L. Lundgren, P. Nordblad, P. Svedlindh, J. A. Cowen, and G. G. Kenning, Phys. Rev. B 40, 869 (1989).
- [86] G. G. Kenning, J. M. Slaughter, and J. A. Cowen, Phys. Rev. Lett. 59, 2596 (1987).
- [87] G. G. Kenning, J. Bass, W. P. Pratt, Jr., D. Leslie-Pelecky, L. Hoines, W. Leach, M. L. Wilson, R. Stubi and J. A. Cowen, Phys. Rev. B, 42, 2393 (1990).
- [88] M. Sawicki, T. Dietl, T. Skoskiewicz, G. Karczewski, T. Wojtowicz And J. Kossut, Acta Phys. Pol. A 88, 1038 (1995).
- [89] P. Granberg, P. Nordblad, P. Svedlindh, L. Lundgren, R. Stubi, G. G. Kenning, D. L. Leslie-Pelecky, J. Bass, J. Cowen, J. App. Phys. 67, 5252 (1990).

- [90] M. Alba, M. Ocio and J. Hammann, *Euro Phys Lett.***2**, 45 (1986).
- [91] M. Alba, J. Hammann, M. Ocio, and Ph. Refregier, H. Bouchiat, *J. of App. Phys.* 61, 3683 (1987)
- [92] G. Parisi, *J. Phys. A: Math. Gen.* 13, 1101 (1980).
- [93] M. Mézard, G. Parisi, N. Sourlas, G. Toulouse, and M. Virasoro, *J. Phys.* 45, 843 (1984).
- [94] Albeit for different reasons. In the film, the crossover to a dimension less than the LCD prevents further domain growth even though there is space to grow unhindered in the in plane direction. The bulk sample, on the other hand, is comprised of crystallites which provide a physical boundary to further domain growth.
- [95] J. Clarke and A. I. Braginski, *The SQUID Handbook*, (Wiley, Weinheim, 2004), Sec. 5.6.
- [96] D. M. Tennant and G. G. Kenning, in production
- [97] We find low frequency *barometric* fluctuations to be the dominant source of SQUID drift further reinforcing our belief in the accuracy of the last points of the TRM. See [96] for a full discussion.
- [98] M. Sasaki, V. Dupuis, J.-P. Bouchaud, E. Vincent, *Eur. Phys. J. B* 29, 469 (2002).

- [99] E. Vincent, J.-P. Bouchaud, D.S. Dean, J. Hammann, Phys. Rev. B 52, 1050 (1995).
- [100] J.-P. Bouchaud, V. Dupuis, J. Hammann, E. Vincent, Phys. Rev. B 65, 024439 (2001).
- [101] A. J. Bray and M. A. Moore, Phys. Rev. Lett. 58, 57 (1987).
- [102] S. R. McKay, A. N. Berker and S. Kirkpatrick, Phys. Rev. Lett. 48, 767 (1982).
- [103] K. Jonason, E. Vincent, J. Hammann, J.-P. Bouchaud, and P. Nordblad, Phys. Rev. Lett. 81, 3243 (1998).
- [104] M. Lederman, R. Orbach, J. M. Hammann, M. Ocio, and E. Vincent, Phys. Rev. B 44, 7403 (1991).
- [105] G. G. Kenning, G. F. Rodriguez, and R. Orbach, Phys. Rev. Lett. 97, 057201 (2006).

Vita

Daniel Moncrief Tennant was born in Austin, Texas on 19 February 1981, the son of Richard and Aimee Tennant. He received the Bachelor of Science degree in Physics from the University of Texas at Austin in 2003. Afterwards, he served as a Peace Corps Volunteer from 2003 to 2005 in Malawi. Upon returning to the States, he entered California State University, Fresno and completed a Masters in Physics in 2008. His thesis, ‘Scattering of Light in Born-Infeld Electrodynamics’ was awarded Thesis of the Year for the university. He then taught as an Adjunct Professor in the Physics Department of Austin Community College from 2009 to 2012. During this time, he made ACC’s first research contribution to *Physical Review* as well as co-sponsored a NASA grant awarded research project. Daniel Moncrief Tennant applied to the Physics graduate program at the University of Texas and began his studies there in the fall of 2011.

Permanent address: 5300B Duval
Austin, Texas 78751

This dissertation was typeset with L^AT_EX[†] by the author.

[†]L^AT_EX is a document preparation system developed by Leslie Lamport as a special version of Donald Knuth’s T_EX Program.